Title of Thesis

Risk Assessment for Heavy Rainfall-Induced Geohazards using Surrogate Models

March, 2025

Shiying ZHENG

Graduate School of

Environmental and Life Science

(Doctor's Course)

OKAYAMA UNIVERSITY

Acknowledgements

Upon completion of this dissertation, I would like to express my sincere gratitude to those who have supported me throughout my academic journey.

First and foremost, I am deeply appreciating to my supervisors, Prof. Nishimura, Prof. Shibata, Prof. Shuku and Prof. Fukumoto. Particularly, I would like to extend my heartfelt thanks to Prof. Nishimura for the five years of guidance from master's to doctoral studies. Your scholarly dedication, research enthusiasm, and rigorous academic attitude have profoundly influenced my development as a researcher.

I am deeply grateful to all my laboratory colleagues in Environmental Infrastructures Laboratory for their support in both research and life. The collaborative spirit and friendship we shared have created cherished memories throughout my doctoral journey. Your companionship and assistance have made these years truly memorable and meaningful.

Finally, my deepest appreciation goes to my family, partner, and friends. Your unwavering support and encouragement have been the strongest foundation for completing my academic pursuits. Your understanding and patience during my long hours of research and writing have given me the strength to persevere. This accomplishment would not have been possible without your constant support.

Abstract

Earth-fill dams play a vital role in agricultural communities, particularly in regions with limited rainfall or without major river systems. These structures, predominantly found in Japan, serve multiple functions including ensuring irrigation water supply, preserving biodiversity, and providing flood protection. However, in recent years, global climate change has led to an increased frequency of extreme weather events, notably intense short-duration rainfall, which significantly elevates the risk of dam failure. Overtopping represents the most common failure mode, often exacerbated by inadequate spillway capacity due to aging infrastructure and insufficient maintenance. Such failures can result in catastrophic consequences for downstream areas, including substantial property damage and potential damage cost of life. Consequently, comprehensive risk assessment of aging earth-fill dams has become imperative. This assessment framework encompasses three critical components: exposure assessment, which quantifies the potential inundation area downstream; vulnerability assessment, which evaluates the resilience of structures and populations to flooding, both contributing to the overall damage cost estimation; and hazard assessment, which determines the probability of overtopping under various rainfall conditions. Traditional quantitative risk assessment methods, while thorough, are often time-consuming, labor-intensive, and costly, limiting their effectiveness in providing timely information for decision-making. Therefore, developing efficient risk surrogate models represents a crucial step toward enhancing the management and safety of these essential hydraulic structures.

This doctoral dissertation proposes an efficient approach to rapidly assess the overtopping probability and potential damage costs of earth-fill dams through the development of surrogate models. Three distinct modeling approaches were employed: Response Surface Method (RSM), Gaussian Process Regression (GPR), and eXtreme Gradient Boosting (XGBoost). RSM provides a traditional statistical framework for approximating the complex relationship between input variables and output variable. GPR, known for its ability to capture uncertainty in predictions, offers probabilistic estimates of dam failure risks. XGBoost, a powerful machine learning algorithm, demonstrates superior predictive capabilities in modeling both the probability of overtopping and associated damage costs. The predictive performance of each model was quantified by comparing their results against detailed method (traditional quantitative risk assessment). XGBoost consistently outperformed other methods based on key performance metrics, including the coefficient of determination (R^2) and root mean square error (RMSE). To enhance model interpretability and understand the relative importance of different variables, the SHapley Additive exPlanations (SHAP) algorithm was implemented, providing valuable insights into the key factors driving dam failure risks. This research contributes to the development of efficient and interpretable tools for earth-fill dam risk assessments, enabling rapid decision-making in disaster prevention and mitigation.

TABLE OF CONTENTS

Chapter 1 Introduction

1.1 Research Background

Geologic hazards or geohazards are adverse geologic conditions capable of causing widespread destruction or loss of property and life (Smith, 2013). These hazards involve long-term or short-term geologic processes that originate from internal earth processes, such as earthquakes, volcanic activity and emissions, mass movements, landslides, rockslides, surface collapses, and debris or mud flows (UNDRR, 2024; NGI, 2024). Figure 1-1 illustrates the formation of some common geologic hazards. Among various triggering factors of geohazards, climate change has emerged as a significant contributor in recent decades. According to IPCC (2023), the average global surface temperature has increased by 1.1°C in the last decade and will reach extremes in 2023. This warming has intensified the global hydrological cycle, leading to increased frequency and severity of extreme weather events, including heat waves,

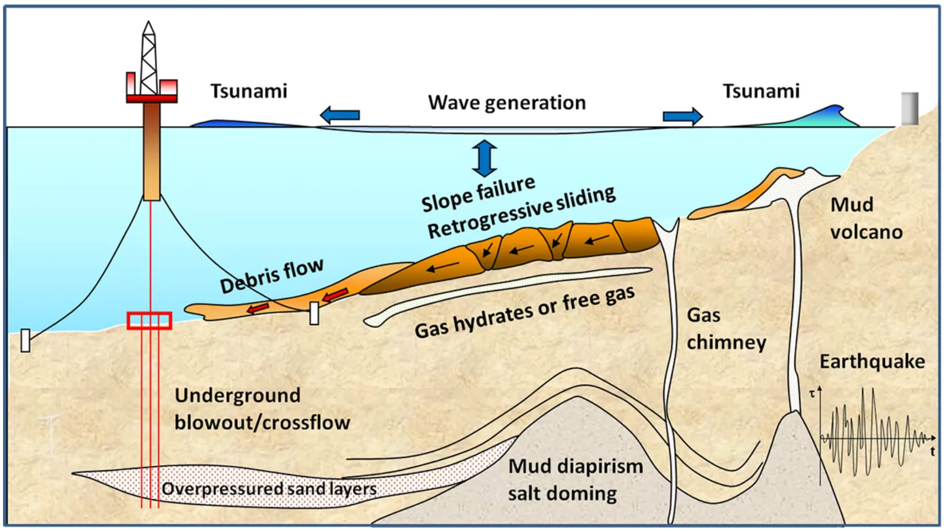

Figure 1-1. Definition of geohazards.
Source: NGI, 2024. https://www.ngi.no/en/research-and-consulting/offshore-container/offshore-geohazards/

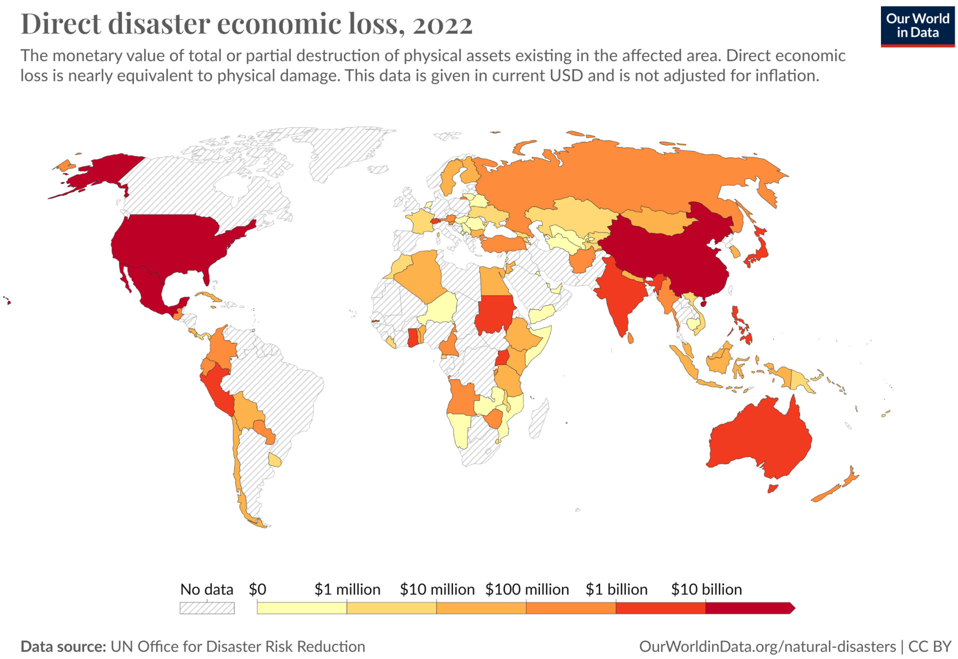

(a) Direct disaster economic loss in 2022

Source: UN Office for Disaster Risk Reduction

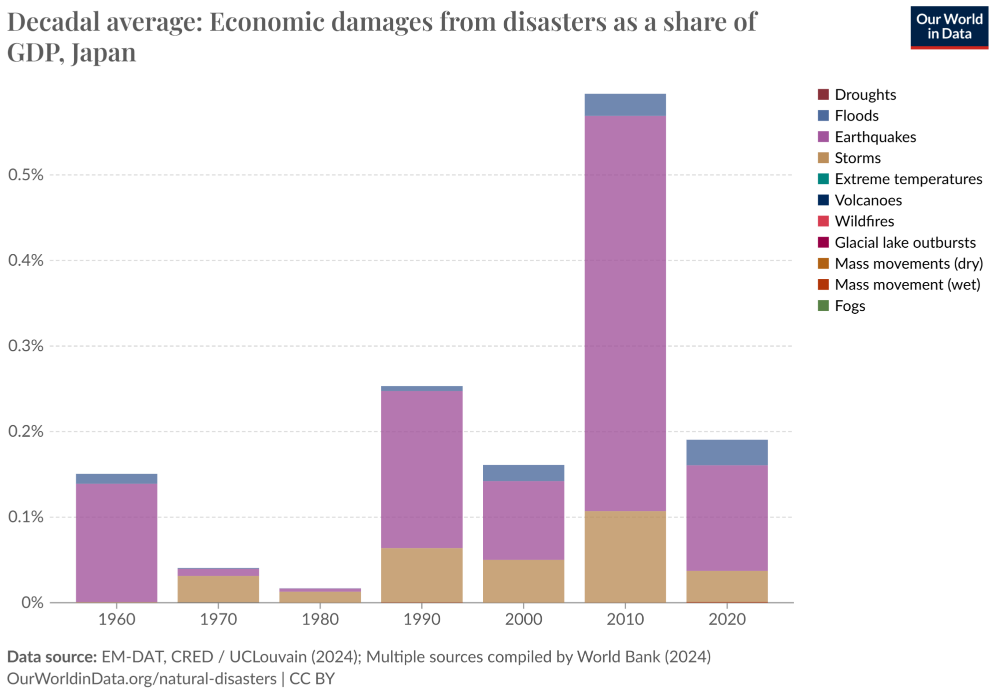

(b) Economic damages from disaster in Japan

Source: EM-DAT, CRED / UCLouvain (2024): Multiple sources compiled by World Bank (2024)

Figure 1-2. Global and Japanese economic losses due to geologic disasters.

cold waves, heavy rainfall, and droughts. Particularly concerning is the rise in flood events, which now account for 44% of all disasters globally (United Nations, 2020).

Japan, situated along the Pacific Ring of Fire, is particularly vulnerable to geohazards due to its frequent tectonic activities. Earthquakes represent the most frequent natural disaster in the country, with the 2011 Great East Japan Earthquake being the most powerful in Japan's recorded history, accompanied by devastating aftershocks and tsunamis that resulted in numerous casualties and extensive property damage (Fire and Disaster Management Agency, 2021). Additionally, extreme weather events have also caused significant disasters, as evidenced by the 2018 Western Japan Heavy Rain event, which led to river flooding, inundation, and sediment-related disasters, including the failure of earth-fill dams resulting in casualties (Cabinet Office, 2018). Figure 1-2 lists the global economic losses due to geohazards in 2022, as collated by UNDRR and EM-DAT, as well as the Japanese GDP losses. These events underscore the critical importance of regional geohazard risk assessment, particularly for water management infrastructure such as aging earth-fill dams.

1.2 Overview of Earth-fill Dam Risk Assessment

Earth-fill dam is typically man-made infrastructures, and the oldest dam made by compacting soil. It is constructed as a simple embankment of well-compacted earth as the most-built dam, accounting for about 70% of the world’s dams. They can be cost-effective in regions where the cost of producing or bringing in concrete would be prohibitive due to could be constructed from local materials. The purpose of earth-fill dams is regulating water in reservoirs to irrigate rural areas, generate electricity, supply water for domestic and industrial use, regulate river levels and flooding downstream of the dam, etc. (ICOLD, 2024).

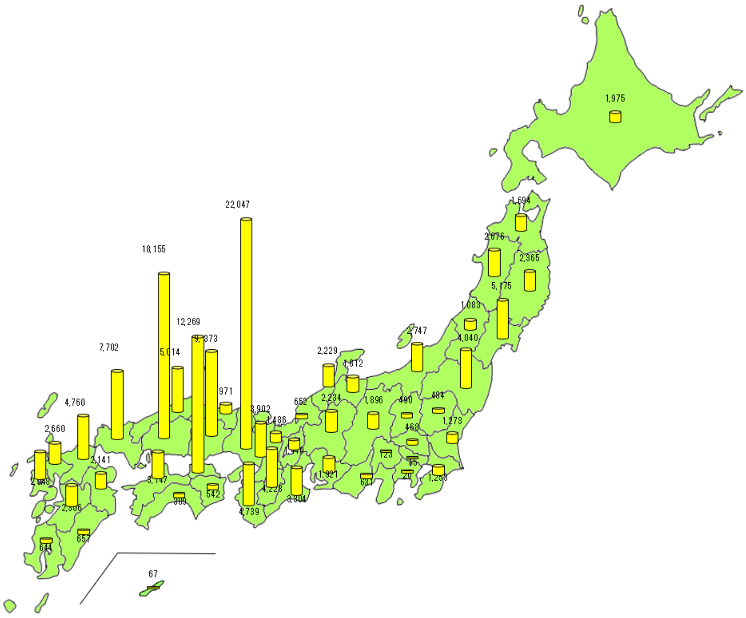

Figure 1-3. Distribution of earth-fill dams in Japan.

There are approximately 150,000 earth-fill dams across Japan, with the majority concentrated in Western Japan. The Setouchi region, which experiences low annual precipitation, has historically relied on these reservoirs, accounting for about 60% of the nation's total (Fig. 1-3). Most of these structures were built before 1850 and have long served not only as vital water sources for agriculture but also as important facilities for disaster prevention (MAFF, 2021). However, their age and deteriorating conditions greatly increase their vulnerability to damage during flooding or earthquakes. This risk was starkly demonstrated during the Heavy Rain Event of July 2018, which resulted in numerous dam failures. In response, emergency inspections of reservoirs nationwide were conducted in cooperation with prefectural governments to implement necessary measures (MAFF, 2021). Given these circumstances, conducting comprehensive risk assessments for these aging earth-fill dams has become an urgent priority.

Dam failure causes include internal erosion, overtopping, structural failure, and overtopping failure is the most frequent under rainfall condition (Fig. 1-4). The factors that cause dam breaches after heavy rains include shear failure, overtopping failure, and piping failure. Previous studies have attempted to analyse earth-fill dam safety by combining both overtopping and piping failure modes. However, results indicated that the contribution of piping to overall failure risk was minimal and could be considered negligible compared to overtopping effects (Nishimura, 2024). The contribution of shear failure to dam breaches is significantly smaller than that of overtopping failures (Shibata et al., 2021). Since overtopping is the major cause of dam breaches (Fujii et al., 1991; ICLOD, 2013), this factor alone is considered in the present paper for simplicity.

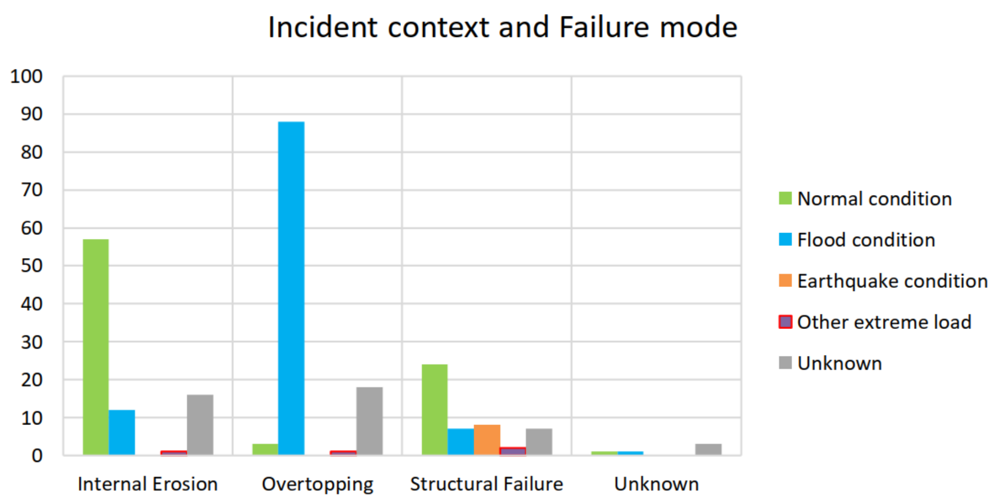

Figure 1-4. Number of embankment dam failures categorized by failure mode and incident context.

1.3 Literature Review

A flood risk assessment is the process of identifying hazards, evaluating the existing vulnerability, and analysing their combined impact. This process determines the nature and extent of risks to exposed elements. Hazards refer to potentially damaging events or phenomena, while vulnerability describes the capacity of individuals or groups to anticipate, cope with, resist, and recover from such events (Schneiderbauer, 2004; Kron, 2005; Merz et al., 2014). Mapping the result of a susceptibility analysis provides initial information on the spatial hazard distribution (Kourgialas & Karatzas, 2011; Chapi et al., 2017) and involves investigating the relationship between environmental factors (topography, geomorphology, soil type, etc.) and triggering factors (rainfall, earthquakes, volcanic eruptions, etc.) in relation to the occurrence of geohazards (Pradhan et al., 2023; Huang et al., 2023). Based on the results, either a qualitative or quantitative flood risk analysis is then undertaken.

Within the broader background of flood risk assessments, dam failure due to flooding has gained significant attention, integrating dam safety assessments (Xu et al., 2023; Lu et al., 2024), economic damage cost estimations, and comprehensive risk assessments. Mathematical models, like DAMSBREACH, have enhanced the simulation of the dam failure process, particularly for cascade reservoirs (Zhou, 2020). Dam overtopping probability assessments have evolved from conditional reliability methods, combining the rainfall threshold theory and Monte Carlo simulations (Sharafati, 2018), the bivariate flood frequency analysis, using copula functions (Liu et al., 2018), and probability-based methodologies, accounting for wind speed and peak flood uncertainties (Hsu, 2010). Dam damage cost assessments have evolved from traditional statistical methods to comprehensive approaches. These include risk assessment systems that incorporate gate failure and flood randomness (Zhang and Tan, 2014), and methods that consider both hydrodynamic and social factors for loss of life calculations (Ge et al., 2021). Recent research emphasizes the importance of time-dependent changes in dam conditions and environments, recognizing the dynamic nature of dam failure risks (Larruari and Lall, 2020). Despite these advancements, current research often lacks a comprehensive, regional-scale approach that can consider multiple independent dams within a given area, combine hydrological modelling with damage cost estimations, and provide quantitative risk assessments.

In recent years, with the ever-increasing power of computers, machine learning (ML) techniques have been applied in natural hazard fields by researchers (Karpatne et al., 2018; Xiao et al., 2022), e.g., susceptibility modelling (Tehrany et al., 2015; Khosravi et al., 2019; Merghadi et al., 2021), anomaly detection (Salazar et al., 2017; Rong et al., 2024), flood modelling (He et al., 2023; Pianforni et al., 2024), and risk assessments (Wang and Zhang, 2017; Darabi et al., 2019; Tang et al. 2022). Particularly, Gaussian Process Regression (GPR) and Ensemble learning methods, like eXtreme Gradient Boost (XGBoost) (Chen, 2016), have emerged as powerful and versatile machine learning techniques (Sun et al., 2014; Bonakdari et al., 2019). GPR outperforms in terms of quantifying uncertainties and providing probabilistic outputs, making it valuable for hydrological and dam safety studies, including flood frequency estimation and dam displacement forecasting (Alexander et al., 2016; Lin et al., 2019). XGBoost, on the other hand, demonstrates superior performance in terms of handling complex environmental data and offering high predictive accuracy and interpretability in flash flood risk assessment, urban flooding susceptibility analysises, and landslide susceptibility mapping (Costache et al., 2022; Ma et al., 2021). Furthermore, the development of explainable machine learning techniques, such as the SHAP (SHapley Additive exPlanations) algorithm, has enabled the interpretation of black-box models, like XGBoost, providing insights into their internal operations and enhancing their applicability in specific research fields (Wang et al., 2023).

1.4 Research Objectives

The traditional risk quantification methods (i.e., detailed method) for assessing overtopping risk of earth-fill dams is time-consuming and labor-intensive. Given the large number of aging earth-fill dams requiring urgent renovation in the study area, it is impractical to quantify risk for each earth-fill dam using detailed method. Therefore, this dissertation aims to develop surrogate models based on influencing factors in the risk quantification, enabling efficient and robust overtopping risk assessment for earth-fill dams.

1.Development of Comprehensive Risk Assessment Framework. This study presents a detailed risk assessment framework for earth-fill dam overtopping, applied to 70 aging dams in Okayama and Hiroshima Prefectures. The framework integrates numerical simulation using the Finite Volume Method to model inundation areas and water depths, considering dam capacity and surrounding topography. The assessment incorporates land use patterns, population distribution, agricultural areas, and building vulnerability characteristics to quantify potential losses. Probability estimation is achieved through Gumbel statistical modeling of rainfall data from local meteorological stations, simulating dam discharge variations. This comprehensive approach provides precise risk assessments that can inform governmental flood management decisions.

2. Implementation of Efficient Surrogate Models. Given the impracticality of applying traditional risk quantification methods to over 4,000 aging dams in Okayama Prefecture alone, this study develops efficient surrogate models. Key influencing factors for loss amount and failure probability are identified through sensitivity analysis. Three modelling approaches are implemented: Response Surface Methodology, Gaussian Process Regression, and XGBoost. Model performance is

evaluated using the coefficient of determination (R^2) and Root Mean Square Error (RMSE), demonstrating the feasibility of rapid and robust risk assessment.

3. Analysis of Risk-Influencing Factors. The study quantifies the contribution of various factors using SHAP values in the surrogate models. Results indicate that water storage is the dominant factor positively influencing loss amounts, while design discharge shows significant negative correlation with failure probability. These findings align with physical mechanisms, where water storage determines inundation extent and design discharge serves as a failure threshold, providing valuable insights for practical applications.

1.5 Outline of the thesis

This dissertation consists of five chapters.

Chapter 1 establishes the research background by examining the increasing frequency of floods due to global climate change, which creates favourable conditions for earth-fill dam overtopping. It then reviews the current status, geographical distribution, significance, primary failure modes, and challenges of earth-fill dams, followed by an analysis of various geological hazards, their triggering mechanisms, and consequent impacts. The chapter concludes with a comprehensive comparison of different surrogate models and their applications in risk assessment.

Chapter 2 focuses on the study areas in Okayama and Hiroshima, Japan, providing detailed information about their geographical locations, environmental factors, geological conditions, and the distribution of earth-fill dams, along with a summary of rainfall monitoring stations for the selected study objects.

Chapter 3 presents the methodology, beginning with traditional risk quantification methods that combine numerical simulation of affected areas and specific damage cost calculations with statistical models for probability estimation based on rainfall data. This is followed by the development of surrogate models using response surface methodology and machine learning algorithms, incorporating selected influencing factors to predict damage costs and occurrence probabilities.

Chapter 4 presents the research result. First discussing the risk assessment results from traditional detailed method and the subsequent ranking of earth-fill dams, then analysing the damage cost and occurrence probabilities derived from both response surface method and machine learning algorithms, such as Gaussian Process Regression and XGBoost.

Chapter 5 provides a comprehensive discussion and conclusion, evaluating the risk quantification results and influencing factors, acknowledging research limitations, and suggesting directions for future research.

Reference

Alexander, M., Priest, S., & Mees, H. (2016). A framework for evaluating flood risk governance. Environmental Science & Policy, 64, 38-47.

Bonakdari, H., Ebtehaj, I., Samui, P., & Gharabaghi, B. (2019). Lake water-level fluctuations forecasting using minimax probability machine regression, relevance vector machine, Gaussian process regression, and extreme learning machine. Water Resources Management, 33, 3965-3984.

Chapi, K., Singh, V. P., Shirzadi, A., Shahabi, H., Bui, D. T., Pham, B. T., & Khosravi, K. (2017). A novel hybrid artificial intelligence approach for flood susceptibility assessment. Environmental modelling & software, 95, 229-245.

Chen, T., & Guestrin, C. (2016, August). Xgboost: A scalable tree boosting system. In Proceedings of the 22nd acm sigkdd international conference on knowledge discovery and data mining (pp. 785-794).

Costache, R., Ali, S. A., Parvin, F., Pham, Q. B., Arabameri, A., Nguyen, H., ... & Anh, D. T. (2022). Detection of areas prone to flood-induced landslides risk using certainty factor and its hybridization with FAHP, XGBoost and deep learning neural network. Geocarto International, 37(25), 7303-7338.

Darabi, H., Choubin, B., Rahmati, O., Haghighi, A. T., Pradhan, B., & Kløve, B. (2019). Urban flood risk mapping using the GARP and QUEST models: A comparative study of machine learning techniques. Journal of hydrology, 569, 142-154.

Fujii, H., Shimada, K., Nishimura, S. (1991): Disaster of earth-fill dams in Okayama Prefecture caused by Typhoon 9019, Research and study on wind and flood damage caused by Typhoon No. 19 in 1990, pp. 101-130.

Ge, W., Wang, X., Li, Z., Zhang, H., Guo, X., Wang, T., ... & Van Gelder, P. (2021). Interval analysis of the loss of life caused by dam failure. Journal of Water Resources Planning and Management, 147(1), 04020098.

He, J., Zhang, L., Xiao, T., Wang, H., & Luo, H. (2023). Deep learning enables super-resolution hydrodynamic flooding process modeling under spatiotemporally varying rainstorms. Water Research, 239, 120057.

Hsu, Y. C., Tung, Y. K., & Kuo, J. T. (2011). Evaluation of dam overtopping probability induced by flood and wind. Stochastic Environmental Research and Risk Assessment, 25, 35-49.

Huang, F., Xiong, H., Yao, C., Catani, F., Zhou, C., & Huang, J. (2023). Uncertainties of landslide susceptibility prediction considering different landslide types. Journal of Rock Mechanics and Geotechnical Engineering, 15(11), 2954-2972.

ICOLD. (2013). Internal erosion of existing dams, levees and dikes, and their foundations.

International Commission on Large Dams. Role of dams. https://www.icold-cigb.org/GB/dams/role_of_dams.asp

IPCC. (2023). Climate Change 2023: Synthesis Report. Contribution of Working Groups I, II and III to the Sixth Assessment Report of the Intergovernmental Panel on Climate Change.

Karpatne, A., Ebert-Uphoff, I., Ravela, S., Babaie, H. A., & Kumar, V. (2018). Machine learning for the geosciences: Challenges and opportunities. IEEE Transactions on Knowledge and Data Engineering, 31(8), 1544-1554.

Khosravi, K., Shahabi, H., Pham, B. T., Adamowski, J., Shirzadi, A., Pradhan, B., ... & Prakash, I. (2019). A comparative assessment of flood susceptibility modeling using multi-criteria decision-making analysis and machine learning methods. Journal of Hydrology, 573, 311-323.

Larruari, P. C., & Lall, U. P. M. A. N. U. (2020). Assessing the exposure of critical infrastructure and other assets to the climate induced failure of aging dams in the US. Final Report for the Global Risk Institute.

Lin, C., Li, T., Chen, S., Liu, X., Lin, C., & Liang, S. (2019). Gaussian process regression-based forecasting model of dam deformation. Neural Computing and Applications, 31, 8503-8518.

Liu, Z., Xu, X., Cheng, J., Wen, T., & Niu, J. (2018). Hydrological risk analysis of dam overtopping using bivariate statistical approach: a case study from Geheyan Reservoir, China. Stochastic Environmental Research and Risk Assessment, 32, 2515-2525.

Ma, M., Zhao, G., He, B., Li, Q., Dong, H., Wang, S., & Wang, Z. (2021). XGBoost-based method for flash flood risk assessment. Journal of Hydrology, 598, 126382.

Merghadi, A., Yunus, A. P., Dou, J., Whiteley, J., ThaiPham, B., Bui, D. T., ... & Abderrahmane, B. (2020). Machine learning methods for landslide susceptibility studies: A comparative overview of algorithm performance. Earth-Science Reviews, 207, 103225.

Ministry of Agriculture, Forestry and Fisheries (MAFF). (2021). Situation of the damaged earth-fill dams due to natural disasters.

NGI. (2024). Offshore geohazards. https://www.ngi.no/en/research-and-consulting/offshore-container/offshore-geohazards/

Nishimura, S. I., Kubota, G., Ohashi, R., Shibata, T., & Shuku, T. (2023). Effect of Permeability Random Field on Piping Risk of a River Dike. In Geo-Risk 2023 (pp. 54-63).

Pianforini, M., Dazzi, S., Pilzer, A., & Vacondio, R. (2024). Real-time flood maps forecasting for dam-break scenarios with a transformer-based deep learning model. Journal of Hydrology, 635, 131169.

Pradhan, B., Dikshit, A., Lee, S., & Kim, H. (2023). An explainable AI (XAI) model for landslide susceptibility modeling. Applied Soft Computing, 142, 110324.

Rong, Z., Pang, R., Xu, B., & Zhou, Y. (2024). Dam safety monitoring data anomaly recognition using multiple-point model with local outlier factor. Automation in Construction, 159, 105290.

Salazar, F., Morán, R., Toledo, M. Á., & Oñate, E. (2017). Data-based models for the prediction of dam behaviour: a review and some methodological considerations. Archives of computational methods in engineering, 24, 1-21.

Schneiderbauer, S., & Ehrlich, D. (2004). Risk, hazard and people's vulnerability to natural hazards. A review of definitions, concepts and data. European Commission Joint Research Centre. EUR, 21410, 40.

Sharafati, A., & Azamathulla, H. M. (2018). Assessment of dam overtopping reliability using SUFI based overtopping threshold curve. Water Resources Management, 32, 2369-2383.

Shibata, T., Nishimura, S., Tateishi, T., Kuroda, S., Kato, T., Kuribayashi, K., Tanaya, N. (2021). Case History of Risk Evaluation of Earth-Fill Dams Due to Heavy Rain, International Journal of Geoengineering Case History, 6(4), 85-100.

Smith, K. (2013). Environmental hazards: assessing risk and reducing disaster. Routledge.

Sun, A. Y., Wang, D., & Xu, X. (2014). Monthly streamflow forecasting using Gaussian process regression. Journal of Hydrology, 511, 72-81.

Tang, X., Chen, A., & He, J. (2022). A modelling approach based on Bayesian networks for dam risk analysis: Integration of machine learning algorithm and domain knowledge. International Journal of Disaster Risk Reduction, 71, 102818.

Tehrany, M. S., Pradhan, B., Mansor, S., & Ahmad, N. (2015). Flood susceptibility assessment using GIS-based support vector machine model with different kernel types. Catena, 125, 91-101.

UNDRR. (2024). Definition: Hazard. https://www.undrr.org/terminology/hazard

United Nations Office for Disarmament Affairs. (2020). Human Cost of Disasters, United Nations.

Wang, F., & Zhang, Q. L. (2017). Systemic estimation of dam overtopping probability: Bayesian networks approach. Journal of Infrastructure Systems, 23(2), 04016037.

Wang, M., Li, Y., Yuan, H., Zhou, S., Wang, Y., Ikram, R. M. A., & Li, J. (2023). An XGBoost-SHAP approach to quantifying morphological impact on urban flooding susceptibility. Ecological Indicators, 156, 111137.

Xiao, T., Zhang, L. M., Cheung, R. W. M., & Lacasse, S. (2022). Predicting spatio-temporal man-made slope failures induced by rainfall in Hong Kong using machine learning techniques. Géotechnique, 73(9), 749-765.

Xu, M., Pang, R., Zhou, Y., & Xu, B. (2023). Seepage safety evaluation of high earth-rockfill dams considering spatial variability of hydraulic parameters via subset simulation. Journal of Hydrology, 626, 130261.

Zhang, S., & Tan, Y. (2014). Risk assessment of earth dam overtopping and its application research. Natural hazards, 74, 717-736.

Zhou, X., Chen, Z., Zhou, J., Guo, X., Du, X., & Zhang, Q. (2020). A quantitative risk analysis model for cascade reservoirs overtopping: principle and application. Natural Hazards, 104, 249-277.

内閣府. (2018). "平成 30 年台風第 7 号及び前線等による被害状況等について"

総務省消防庁. (2021). 平成 23 年(2011 年)東北地方太平洋沖地震（東日本大震災）について（第 150 報）

Chapter 2 Study Area

This study focuses on Okayama and Hiroshima Prefectures, located in the Chugoku region at the western end of Honshu, Japan. The western region of Japan contains a high concentration of earth-fill dams, with Hiroshima Prefecture ranking second and Okayama Prefecture ranking fourth nationwide in terms of dam numbers. The significance of studying these areas was highlighted by the Western Japan Heavy Rain event in 2018, during which 48 earth-fill dams in Hiroshima Prefecture failed, leading to landslide disasters that resulted in 109 fatalities. Similarly, in Okayama Prefecture, the failure of 4 earth-fill dams contributed to 61 fatalities, with the annual rainfall for that year reaching 216% of the average annual rainfall (Japan Society of Civil Engineers, 2018; Sanyo Shimbun, 2024; Cabinet Office, 2018). These tragic events underscore the critical need for comprehensive risk assessment in these regions. Consequently, this study selected 70 sites from among the aging earth-fill dams requiring urgent renovation to analyze their overtopping failure risks. In this study, we selected rainfall monitoring stations in close proximity to the study sites and collected precipitation data accordingly.

2.1 Okayama prefecture, Japan

Okayama Prefecture is located in the southeastern part of the Chugoku region, covering an area of approximately 7,100 km² (ranked 15th nationally). It serves as a crossroads connecting the San'in, San'yo, and Shikoku regions. The prefecture borders Hyogo Prefecture to the east, Hiroshima Prefecture to the west, and Tottori Prefecture to the north along the Chugoku Mountain range (elevation 1,000-1,200m). Three major rivers - the Yoshii, Asahi, and Takahashi Rivers - originate from the Chugoku Mountains and flow into the Seto Inland Sea. Geologically, the area is characterized by widespread distribution of andesite, granite, and slate, with rhyolite predominantly found in the northwestern and eastern coastal areas. The soil composition varies from brown forest soil in the north to dry brown forest soil in the central region, while the southern coastal areas feature immature soil that has undergone deep weathering. The climate shows significant variation between the northern and southern regions: the average annual temperature ranges from 10-14°C in the north to 14-15°C in the south, while annual precipitation varies from 1,500-1,900mm in the north to 1,000-1,400mm in the south. Snowfall is notable only in the northern region, which experiences a Japan Sea climate pattern with approximately 1m of snow annually, while the southern region receives minimal snowfall (FMC, 2024; Okayama Prefecture, 2024; Okayama-geo, 2024). The distribution of earth-fill dams and geologic map of Okayama prefecture are shown in Figure 2-1.

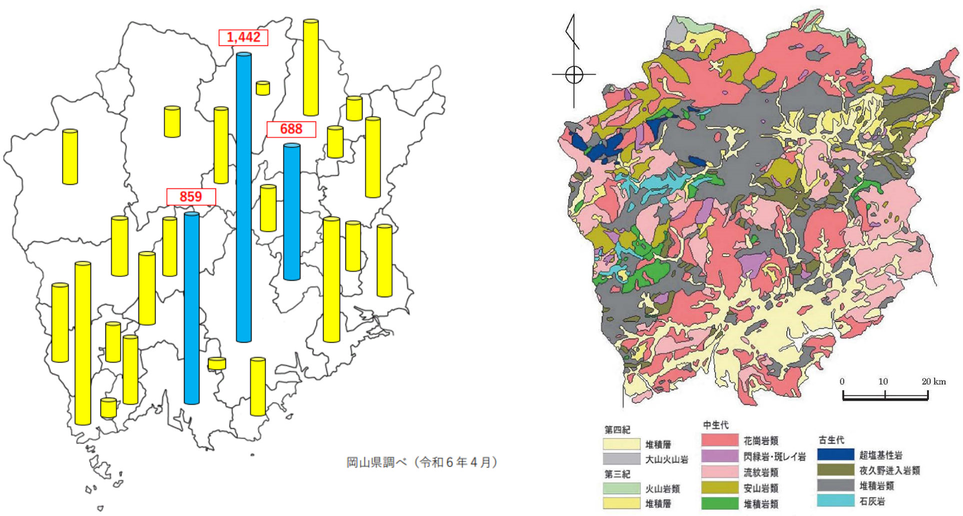

Figure 2-1. Distribution of earth-fill dams and geologic map of Okayama prefecture.
Source: Okayama-geo (2024); MAFF (2024)

2.2 Hiroshima prefecture, Japan

Hiroshima Prefecture is located in the central part of the Chugoku region, covering approximately 8,500 km² (2.2% of Japan's total area). Forest areas account for about 72% of the prefecture's total area, predominantly consisting of private forests. The topography descends from the Chugoku Mountains in the north, where Mount Osorakan stands as the highest peak along the prefectural border, to the Seto Inland Sea in the south, with the northern border ridge area reaching elevations of around 1,000m. The prefecture contains five major river systems: the Takahashi, Ashida, Go, Ota, and Oze Rivers, with a total length of about 2,400 km. Geologically, the area is dominated by acidic rocks, primarily granite and granite porphyry. Granite is the most widely distributed rock type, covering about 40% of the prefecture's area, while igneous rocks including granitic and rhyolitic rocks account for approximately 70% of the total area. The climate varies significantly between coastal and mountainous regions: the coastal areas experience an average annual temperature of 15-16°C with annual precipitation of 1,000-1,100mm, while the mountainous regions have an average annual temperature of 10-11°C with annual precipitation of 2,000-2,400mm. The northern mountainous areas experience cold winters with snowfall accumulation of 1-1.5m (FMC, 2024; Hiroshima Prefecture, 2024). The distribution of earth-fill dams and geologic map of Hiroshima prefecture are shown in Figure 2-2.

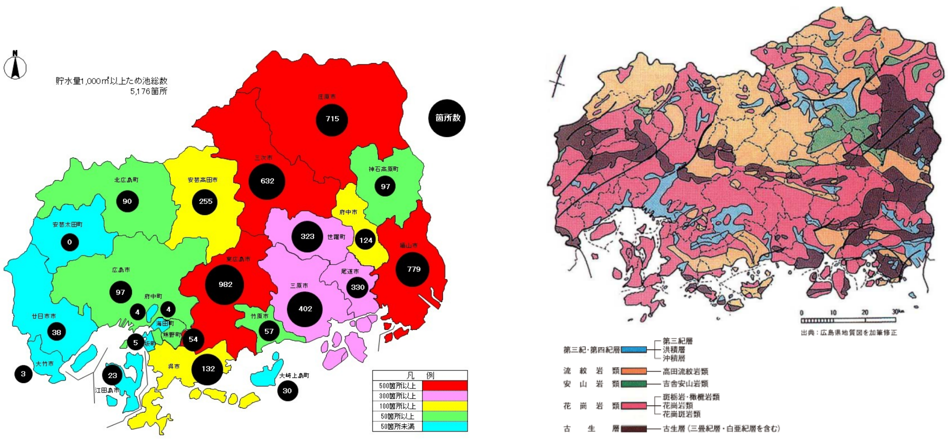

Figure 2-2. Distribution of earth-fill dams and geologic map of Hiroshima prefecture.
Source: FMC (2024); Hiroshima Prefecture (2024)

2.3 Rainfall observation

The Automated Meteorological Data Acquisition System (AMeDAS) in Japan is a regional meteorological observation network that automatically monitors precipitation, wind direction/speed, temperature, and humidity to provide detailed temporal and spatial weather data for disaster prevention and mitigation. The system comprises approximately 1,300 precipitation monitoring stations nationwide (spaced approximately 17 km apart). Of these, about 840 stations (spaced approximately 21 km apart) measure additional parameters including wind direction/speed, temperature, and humidity. In snow-prone regions, approximately 330 stations also monitor snow depth (JMA, 2024a).

In this study, we selected 17 rainfall monitoring stations proximate to the 70 chosen earth-fill dams, located in: Okayama, Hiroshima, Kure, Yakage, Kasaoka, Waki, Tamano, Higashi Hiroshima, Kurashiki, Takehara, Mushiage, Miiri, Kibichuo, Tsushimi, Fukuwatari, Akaiwa, and Shiwa (Figure 2-3). Historical rainfall data from these stations was collected to construct Gumbel distribution for analysis.

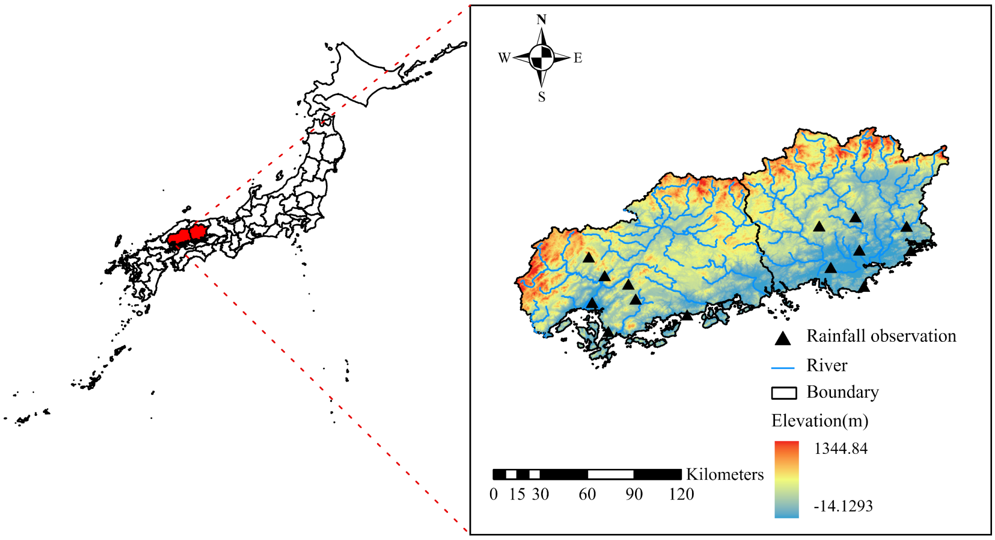

Figure 2-3. Study area and rainfall observation.

Reference

岡山県支部, 中国地質調査業協会: 岡山県の地形. https://okayama-geo.jp/pdf/201211-04.pdf Accessed in December 21, 2024

岡山県: 岡山県の地形と河川. https://www.pref.okayama.jp/page/detail-7206.html Accessed in December 21, 2024

森林整備センター(Forest Research and Management Organization Forest Management Center): 中国四国整備局地勢・地質・気候（岡山県）. https://www.green.go.jp/seibi/chugoku-shikoku/chisei_chishitsu_kiko/okayama.html Accessed in December 21, 2024

森林整備センター: 中国四国整備局地勢・地質・気候（広島県）. https://www.green.go.jp/seibi/chugoku-shikoku/chisei_chishitsu_kiko/hiroshima/hiroshima.html Accessed in December 21, 2024

広島県: 地質概要 - 広島県. https://www.pref.hiroshima.lg.jp/uploaded/attachment/412890.pdf Accessed in December 21, 2024

内閣府. (2018): "平成 30 年台風第 7 号及び前線等による被害状況等について"

山陽新聞社: 西日本豪雨特集. https://c.sanyonews.jp/gou_graph/ Accessed in December 21, 2024

土木学会委員会. (2018): 西日本豪雨における広島県の被害について. https://committees.jsce.or.jp/chugoku/system/files/tutida.pdf

農林水産省 (2024): 岡山県におけるため池の管理保全の取組状況. https://www.maff.go.jp/j/nousin/bousai/bousai_saigai/b_tameike/attach/pdf/tameike_iinkai-52.pdf

国土交通省　気象庁(JMA) (2024a). 地域気象観測システム（アメダス）. https://www.jma.go.jp/jma/kishou/know/amedas/kaisetsu.html

Chapter3 Risk Quantification Methods: Detailed Assessment and Surrogate Model Development

This research employs a two-stage approach to risk assessment. Initially, a traditional risk quantification method (referred to as the detailed method) is applied, which involves simulating inundation areas, collecting downstream land use information to estimate potential damage cost, and calculating overtopping failure probability through dam discharge simulation under varying rainfall conditions. Subsequently, highly sensitive factors are identified and selected as variables for constructing surrogate models. Three different modeling approaches are implemented as surrogate models: response surface methodology (RSM), Gaussian Process Regression (GPR), and eXtreme Gradient Boost (XGBoost), to develop efficient risk assessment tools.

3.1 Risk quantification for earth-fill dams by detailed method

In the evaluation of a single event with potential consequences, the risk is defined as the product of the probability of an event occurring and the consequences of its occurrence (Faber, 2003), as shown in Equation (1). The analysis of the probability of an event occurring is generally referred to as a hazard analysis (Aven, T., 2016), while the analysis of the consequences of its occurrence is referred to as an overall analysis of exposure and vulnerability, which describes the extent of damage to people, property, the environment, or other assets exposed to the threat of geohazards. In this section, the risk is defined by the two above indices.

$$R = C \times P_f \tag{1}$$

where R refers to the risk to an earth-fill dam during flooding, C refers to the damage cost, and P_f refers to the probability of the failure of an earth-fill dam due to overtopping.

To quantify the risks to an earth-fill dam, a detailed method should be used to calculate the damage costs. The following three steps are performed to complete this task.

1. Simulation of downstream inundation areas caused by dam overtopping during floods using the Finite Volume Method

2. Collection of downstream area information including land use types, population distribution, and building infrastructure data

3. Quantification of monetary losses by combining inundation areas and land use information according to the criteria established by the Economic Survey of Water Management

3.1.1 Damage cost

In this paper, the calculation of the damage cost for an earth-fill dam is divided into an exposure analysis and a vulnerability analysis.

The exposure analysis is used to determine the flooding area in the event of overtopping from an earth-fill dam. The two-dimensional shallow water equation is used as the fundamental equation in the flood analysis. To conduct the flood simulation, the assumption of the Riemann problem (Toro 1999), which can deal with the discontinuity of flow, is employed here. The equations are solved by the Finite Volume Method (FVM) (Yoon and Kang 2004), employing two-dimensional rectangular cells. Details of the numerical analysis are provided in Nishimura, et al. (2021). The elevation data for the earth-fill dams and their downstream areas were obtained from the Geospatial Information Authority of Japan by specifying the target three-dimensional cell (1 km x 1 km), basically at 5-meter intervals. However, the flood analysis uses a 25-m unit for each cell, so the obtained elevation data must be arbitrarily thinned out. The water depth per 25-meter cell is obtained from the results of the flood analysis. The information used when calculating the costs of damage is the maximum inundation depth within 9500 seconds after the earth-fill dam breaches. The flood analysis can reproduce the inundation of the earth-fill dam water. Fig. 3-1 (a) shows the boundary of outflow in this study, while Figs. 3.1 (b) and (c) show examples of the maximum submergence depth obtained from the flood simulation at two representative sites.

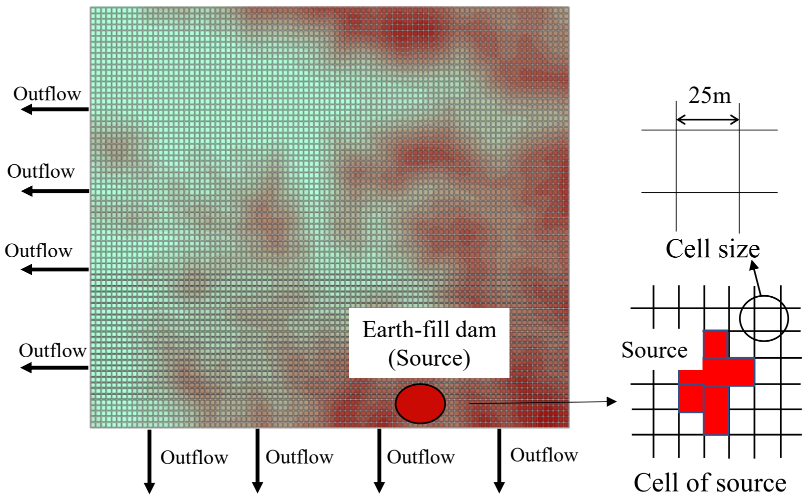

(a) Outflow boundary and cell size.

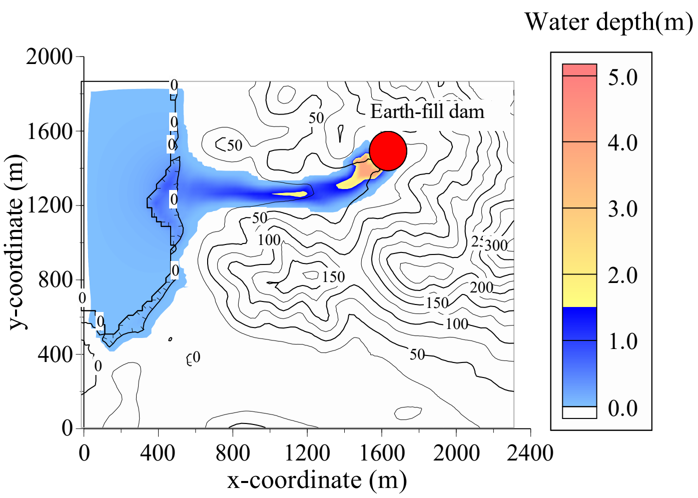

(b) Flood analysis for example.

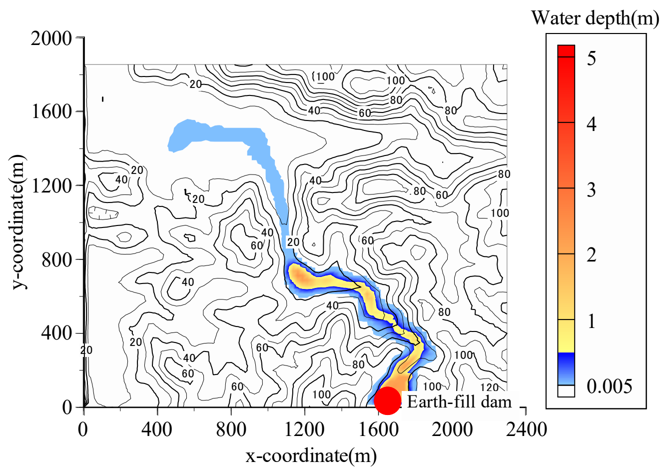

(c) Flood analysis for example

Figure 3-1. Examples of flood analysis.

3.1.2 Land use

The vulnerability analysis is used to quantify the cost of economic losses within the flooding depth. In terms of land use, a method is proposed to calculate the damage costs of the inundation according to the national regulations (Rural Development Bureau of MAFF 2020) by the asset data. Examples of land use are depicted in Fig. 3-2.

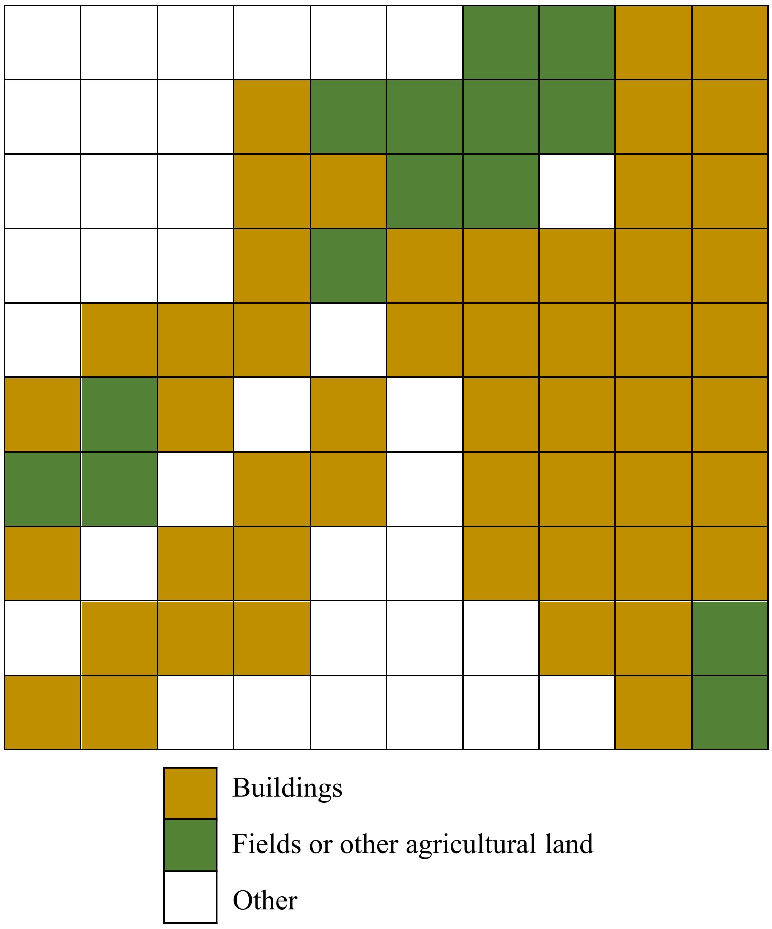

Figure 3-2. Examples of land use.

The evaluation of the damage costs proposed by Shibata, et al. (2021) is employed here. Details method, in which damage is divided into direct damage and indirect damage, are given in Shibata, et al (2021). Direct damage includes damage to assets, such as residences, office buildings, and crops. Indirect damage is the loss due to business suspension and the costs of first-aid measures at home and at business establishments. The inundation depth is obtained from the numerical results of the flood analysis.

The damage to buildings is divided into two categories, namely, residential building damage and office building damage.

Residential building damage= house damage + household furniture damage. (2)

The damage to houses is calculated by multiplying the house assets, floor area, and damage rate as a function of the water depth estimated by the flood analysis.

House damage

= house assets per area × total floor area × number of households per cell

× number of inundated cells × damage rate by inundation depth (3)

House furniture damage is defined as the product of the household furniture assets and the damage rate to the inundation depth.

House furniture damage

= value of house furniture per household × number of households per cell

× number of inundated cells × damage rate by inundation depth (4)

Office building damage consists of the following terms:

Office building damage

= redemption and inventory assets + damage of business suspension and stagnation + cost of emergency measures (5)

The redemption assets and inventory assets are calculated by multiplying the number of employees by the unit price per employee.

Redemption asset damage

= depreciable assets per employee × number of employees per cell

× number of inundated cells × damage rate by inundation depth (6)

Inventory assets damage

= inventory assets per employee × number of employees per cell

× number of inundated cells × damage rate by inundation depth (7)

The damage due to business suspension and stagnation, Dss, is expressed as

$$D_{ss} = M \times \left(n_0 + \frac{n_1}{2} \right) \times p \tag{8}$$

where M is the number of employees, which equals the product of the number of inundated cells and the number of employees per cell, n0 is the number of days of business suspension, n1 is the number of days of stagnation, and p is the additional value divided by the number of persons and days. The days of business suspension and stagnation are shown in Table 3-1.

Table 3-1. Days of business suspension and stagnation.

Inundation depth	Under the floor	Above the floor Under 50 cm	50-99	100-199	200-299	300cm and above
Unit costs/1,000JPY (Households)	82.5	147.6	206.5	275.9	326.1	343.4
Unit costs/1,000JPY (Offices)	470	925	1,714	3,726	6,556	6,619

The cost of emergency measures is determined by Eq. (9).

Cost of emergency measures

= alternative activity expenditure burden in office sector by inundation depth

× number of offices per cell × number of inundated cells (9)

Table 3-2 shows the unit costs of alternative activity expenditure burden for households and offices.

Table 3-2. Unit costs of alternative activity expenditure burden for households and offices.

Inundation depth	Under the floor	Above the floor Under 50 cm	50-99	100-199	200-299	300cm and above
Unit costs/1,000JPY (Households)	82.5	147.6	206.5	275.9	326.1	343.4
Unit costs/1,000JPY (Offices)	470	925	1,714	3,726	6,556	6,619

Paddy field damage and soy damage are calculated as agricultural damage. The inundation area is the product of the number of inundated cells and the cell area.

Paddy field damage

= normal yield per area × unit price of rice

× percentage of crop acreage of paddy field

× inundation area × damage rate by inundation depth (10)

Fig. 3-3 shows examples of the industrial damage costs and agricultural damage costs per $1m^2$ for the example of flooded areas.

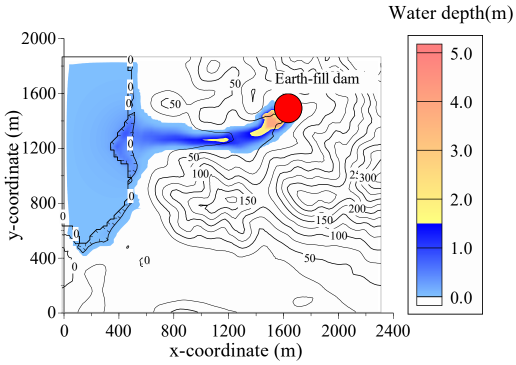

(a) Depth of water (m)

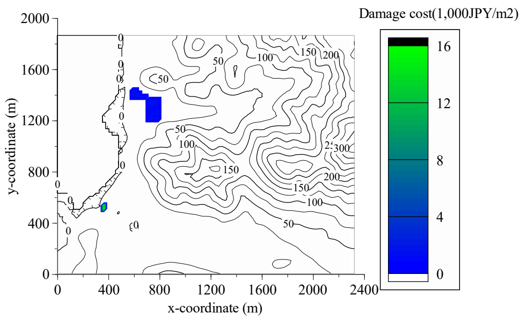

(b) Industrial damage costs (1,000JPY)

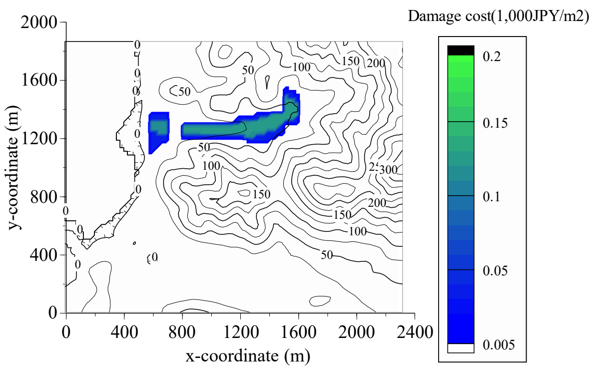

(c) Agricultural damage costs (1,000JPY)

Figure 3-3. Examples of damage costs.

3.1.3 Overtopping probability

In this study, the overtopping probability is defined as the probability that the outflow from an earth-fill dam will exceed the design flow discharge within a certain period, 72 hours of continuous rainfall in this paper. The rainfall data are firstly collected, the return periods are obtained from different rainfall observatories based on the Gumbel distribution, and then the 72-hour change in outflow is calculated based on the storage function method. The annual probability of failure, namely, the probability of failure within the arbitrary one year, is discussed in the manuscript.

Geohazards are rare events, and thus, follow a binomial distribution (Corominas et al., 2014). The average probability of geohazard P occurring per return period T is shown in the following equation:

$$P^{\circ} N=1;t=1 \doteq \frac{1}{T} \tag{11}$$

Eqs. (12) and (13) are used to calculate the peak flood discharge.

$$Q_p = \frac{1}{3.6} A \cdot r_e \tag{12}$$

$$r_e = f_p \cdot r \tag{13}$$

Q_p: peak flood flow rate (m^3/s)

A: catchment area (km2)

re: average effective rainfall intensity within the flood arrival time (mm/hr)

r: rainfall intensity in the catchment area (mm/hr)

f_p: peak outflow coefficient (In this study, f_p is set to 1.)

In this study, the Gumbel distribution predicts the hourly probability of rainfall for each year and obtains the peak flood flow from the hourly probability of rainfall.

This study focuses on the continuous rainfall that fell over the 72-hour period from July 5th to 7th of 2018 as the subject of investigation. In addition, the annual maximum 72-hour rainfall totals for the 45-year period from 1975-2020 were collected for this study as the basis for the calculation of the return period. Rainfall data were obtained from 14 stations (JMA, 2024b) in close proximity to the selected 70 earth-fill dams.

Firstly, the probabilistic model for the annual maximum rainfall of 72 hours of continuous rain is based on the rainfall data records obtained from the observation stations near the earth-fill dam sites in Okayama and Hiroshima. According to the previous cases of breaches, overtopping occurs within 72 hours of heavy rains. Then, using the probability of the occurrence of the heavy rainfall acquired hereafter and the actual rainfall waveform obtained from the heavy rainfall in western Japan in 2018, the probability of overtopping failure in any given year can be calculated.

The Gumbel distribution is an extreme value distribution used in modelling the maximum value by an ordinal statistic. It is widely used in predicting the likelihood of extreme events that could lead to disasters (D. Koutsoyiannis, 2004). The probability density function is shown by the following equation:

$$\begin{aligned} f(x) &= a\exp(-y - e^{-y}) \\ y &= a(x - x_0) \end{aligned} \tag{14}$$

where x is the precipitation (mm/h), a is the location parameter that determines the position of the distribution, and x_0 refers to the scale parameters, which determine the scale or width of the distribution. The two parameters can be calculated as follows:

$$\frac{1}{a} = \frac{S_x}{S_y}$$
$$x_0 = \bar{x} - \frac{\bar{y}}{a} \tag{15}$$

S_x and S_y are the standard variation for x and y. Fig. 3-4 shows the probability of precipitation curve for the rainfall observation site called Tamano.

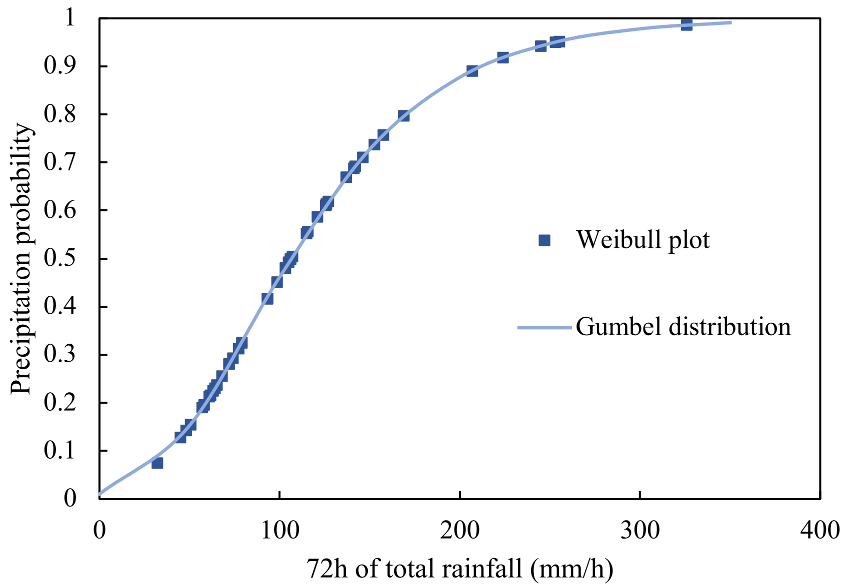

Figure 3-4. Example of 72-hr probability of precipitation curve in Tamano.

It is assumed that the design flood discharge capacity of an earth-fill dam is given by (m^3/s), and that overtopping failure probability is defined by the following equation:

$$P_f = \text{Prob}[Q_d < Q_p] \tag{16}$$

In this study, it is assumed that the earth-fill dams are at the full water level. If the peak flood flow of an earth-fill dam exceeds the designed flood discharge, overtopping will occur, leading to a breach.

From the prepared probability precipitation curves, the annual maximum 72-hr probability of precipitation is extracted, corresponding to the probability of rainfall depicted in Fig. 3-4. The hyetograph for an arbitrary probability, dependent on the probabilistic 72-hr total rainfall derived from Fig. 3-4, can be calculated using Eq. (17). An example of a hyetograph, namely, the time series of the rainfall intensity for the 72-hour probability of precipitation, is presented in Fig. 3-5.

$$I_{prob}(t) = I_{obs}(t)\frac{I_{probD}}{I_{obsD}} \tag{17}$$

where t is the elapsed time, $I_{prob}(t)$ is the probabilistic hyetograph, $I_{obs}(t)$ is the observed hyetograph, I_{probD} is the probabilistic 72-hour precipitation derived from the precipitation probability curve, and I_{probD} is the maximum recorded 72-hour precipitation (mm). The variables, $I_{prob}(t)$ and $I_{obs}(t)$, are assumed to be related linearly in Eq. (17). Since the amount of accumulated rainfall is more important for

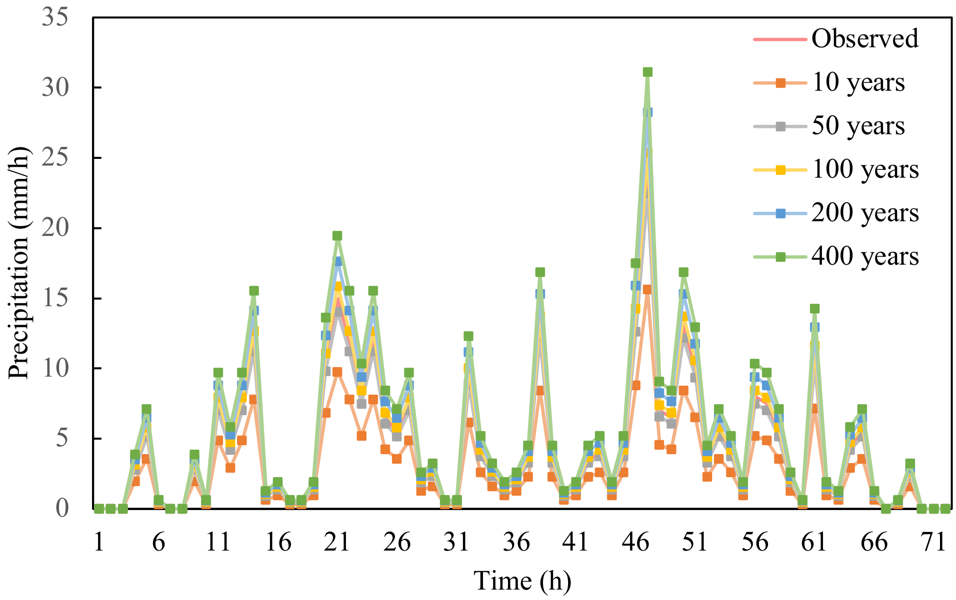

Figure 3-5. Time series of precipitation corresponding to return periods. (Original precipitation was observed at Tamano.)

the dam breaching than the shape of the hyetograph, the simple assumption is adopted for the hyetograph here.

For the breaching of earth-fill dams, the total rainfalls of the sequential periods of precipitation up to 72 hours are sensitive; thus, several hyetographs, which are adjusted so that total rainfalls of 72 hours coincide with those of the probabilistic 72-hour rainfalls, namely, the return periods, are depicted in Fig. 3-5.

To increase the accuracy of the probability of overtopping failure, firstly, the storage function method should be considered. The mean of the term "storage" in this approach is the rainfall once stored in the ground of the catchment area.

To express the non-linear characteristics of the runoff phenomenon, the storage function method introduces a conversion process from rainfall to runoff, assumes a unique functional relationship between the amount of storage and the amount of runoff, and finds the runoff from rainfall using the amount of storage as a parameter.

The storage function model is expressed by the following equations (MAFF 2019):

$$S_l = KQ_l^p \tag{18}$$

$$\frac{dS_l}{dt} = r_e - Q_l \tag{19}$$

Q_l: direct outflow considering the delay time (mm/h)

S_l: storage considering the delay time (mm)

r_e: effective rainfall intensity (mm/h)

Parameter $f_p = 1$ is assumed in Eq. (13) when the storage function method is used.

$$K = \beta \cdot A^{0.14} \tag{20}$$

β=5, P=0.6

Kimura, the proponent of the storage function model (1967), proposed the following equation for mountain basins. Since the stream lengths of the earth-fill dams used in this study are less than 11.9 km, the delay time is set to 0.

$$T_l = 0.047L - 0.56 \quad (L > 11.9 \text{ km}) \tag{21}$$

T_l = 0 ($L \leqq 11.9$ km)

L: stream length (km)

The peak value of Q_l is substituted into Eq. (14) as $r_e = Q_l$ when the storage function method is used.

An example of the 72-hour storage function model in this study is shown in Fig. 3-6. The outflow amount in the figure refers to the rainfall that actually flows into the earth-fill dam.

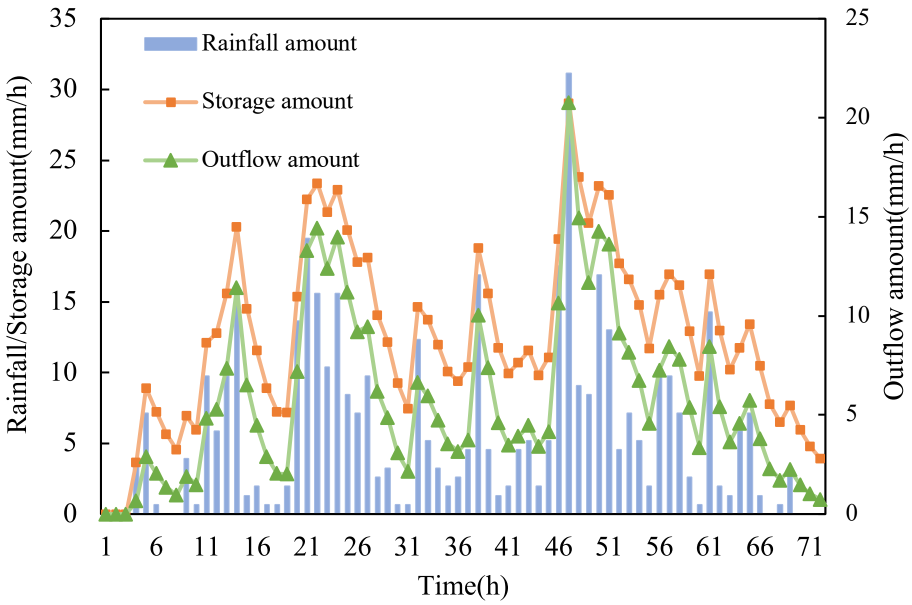

Figure 3-6. Overflow depth of storage function method corresponding to return period of 400 years.
(Site: 1, Observatory: Tamano)

If detailed information on the spillway of a dam can be obtained, it is thought that the storage effect will provide an accurate prediction of the probability of overtopping failure. The storage effect is the additional storage relative to the full water level of the earth-fill dam, that is, the amount of water allowed from the full water level of the earth-fill dam to the critical full water level of the spillway. It can affect the peak overtopping discharge during a continuous rainfall event and the probability of exceeding the runoff height of the earth-fill dam (MAFF 2015). The overtopping probability, considering the storage effect, is defined as Eq. (22).

$$P_f = \mathrm{Prob}[h_d < h_p] \quad (22)$$

h_d: designated overtopping head on the spillway (m)

h_p: peak overtopping head on the spillway (m)

To calculate the marginal overtopping depth, the inflow and outflow must firstly be determined.

$$Q_{in} = \frac{1}{3.6} A \cdot Q_l \tag{23}$$

Eqs. (14) and (16) are used for the dams, from which the correct information for the spillway designs cannot be obtained, while Eqs. (22) and (23) are used for the dams, from which the spillway information is well known. Eqs. (14) and (16) are based on the safety-side assumption, while Eqs. (22) and (23) can estimate the more correct probability.

The discharge equation for a rectangular weir, as used in this study, is

$$Q_{out} = C \cdot B_s \cdot h^{\frac{2}{3}} \tag{24}$$

where Q_{out} is the discharge (m^3/s), C is the discharge coefficient, B_s is the width of the spillway (m), and h is the static or piezometric head on the spillway bottom (m). The values for B_s and C for each earth-fill dam are derived from Rural Areas Disaster Prevention and Mitigation Project (Earth-fill Dams Maintenance) District Overview Document provided by Agriculture, Forestry and Fisheries Department of Okayama Prefecture. The storage of water in the water reservoir, V_r (m^3), is estimated as follows:

$$V_r = A_w h \tag{25}$$

A_w: area of an earth-fill dam (m^2)

There is a constant equivalent relationship among inflow, outflow, and storage.

$$\frac{dV_r}{dt} = Q_{in} - Q_{out} \tag{26}$$

Overtopping depth h is adjusted by an iterative calculation until the above Eqs. (22) – (26) are consistent; then the calculation is repeated for the duration of the rainfall, and the peak overtopping depth, h_p= maximum overtopping head during the rainfall, is determined.

Fig. 3-6 shows an example of the 72-hour sequence water depth for the return period of 400 years. The return period is calculated as the inverse of the probability that the peak overtopping depth, hp, will exceed the design overtopping depth, h_d. In the case of Fig. 3-6, the peak overtopping depth is h_p= 0.4 m.

In order to calculate the probability of overtopping, the storage function method is applied for the sites in both of Hiroshima and Okayama, and the storage effect is applied for the sites only in Okayama since precise information is available for the Okayama sites.

3.2 Parameters for surrogate models

3.2.1 Parameters selection for damage cost and overtopping probability

In this study, so as to construct surrogate models for the damage cost and probability of overtopping, four influential variables were chosen for each model, as shown in Table 3-3.

Table 3-3 Variables chosen in this study.

Surrogate model	Variable name	Unit
Damage cost	Water storage	m^3
	Median slope	/
	Number of households in flooding area	$Household/km^2$
	Number of employees in flooding area	$Employee/km^2$
Probability	Catchment area	km^2
	Water storage	m^3
	Peak rainfall intensity	mm/h
	Design flood discharge	m^3/s

The damage cost calculation was divided into an exposure analysis and a vulnerable analysis. The variables that influence those processes were chosen. They include *V*: effective water storage of the earth-fill dam, *S*: median slope of the main route of the flood water judged from the geometry, *H*: number of households per 1 km^2 of available area in the analytical area, and E: number of employees per 1 km^2 of available area in the analytical area (Mizuma, 2016). We conducted sensitivity analysis based on orthogonal arrays to select four highly influential factors from eight initial factors, followed by Principal Component Analysis (PCA) to examine the relationships between these factors. The specific steps are as follows.

3.2.2 Sensitivity analysis for variables of damage cost

In this study, a sensitivity analysis, based on an orthogonal array as screening, is conducted to determine the factors with the highest sensitivity, based on the concept of experimental design.

The damage costs are calculated by (i) calculating the maximum inundation depth by a flood analysis and (ii) using asset data, such as the number of households, employees, and area of agricultural land for the flood analysis (Mizuma 2016). The factors influencing these processes, like for categories (i) and (ii), are selected.

(i) :

a: effective water storage of the earth-fill dams

b: ratio of the downstream area of the earth-fill dam sites to the total area of the flood analysis. The downstream area is defined as the area below an earth-fill dam's altitude, while the total area is defined as the rectangular analytical area just including the floodable area.

c: median gradient of the main route of the flood water judged from the geometry

(ii):

d: ratio of the area whose type of land use does not correspond to "forest" or "lake", namely, usable area, to the total area of the flood analysis

e: number of households in the available area per 1 km^2 in the analytical area

f: number of employees in the available area per 1 km^2 in the analytical area

g: agricultural area in the available area per 1 km^2 in the analytical area

h: average price of crops in the available area per 1 km^2 in the analytical area

In Equation (10), $\mathbf{x}_R = (a, b, c, d, e, f, g, h)$ is introduced for the regression analysis.

For the sensitivity analysis, three model areas, Site A, Site B, and Site C, are selected to consider the variability of the geometry. The results of the flood analysis are depicted in Fig. 3-3. The effective water storage capacity of the reservoir is the largest at Site A, followed by Site B and Site C. Based on the actual information on the three sites, the maximum, median, and minimum values of factors *a, b, c, d, e, f, g*, and *h* are determined. Then, the maximum, median, and minimum values are assigned to factors *a, b, c, d, e, f, g*, and *h*. In other words, virtual earth-fill dam sites are created by preparing several sets of factors. For the setting of the analytical cases, the damage costs can be obtained. Details of the analysis are presented in Mizuma (2016).

The factors are prepared as an orthogonal array, consisting of columns that are orthogonal to each other. The L_{16} orthogonal array created for the present analysis, based on the experimental design concept, is depicted in Table 3-4. The table presents the 17 analytical patterns, No. 1-No. 17, and shows the damage costs, which are derived from the detailed method. In the table, "1" is the maximum value, "-1" is the minimum value, and "0" is the median value. The values of "1", "0", and "-1" represent the standardized values for the factors in the sensitivity analysis. The analytical patterns for L_{16} consist of a variety of "1" and "-1, and the pattern for the median points of all factors (0, 0, …, 0) is added to the orthogonal array as No. 17.

For example, No. 1 in Table 3-4 consists of ($a_s, b_s, c_s, d_s, e_s, f_s, g_s, h_s$) = (1, 1, 1, 1, 1, 1, 1, 1), while No. 2 consists of ($a_s, b_s, c_s, d_s, e_s, f_s, g_s, h_s$) = (1, 1, 1, 1, -1, -1, -1, -1). The geometry data for Site A are assigned to Nos. 5-8 and Nos. 13-16, those of Site B are assigned to No. 17, and those of Site C are assigned to Nos. 1-4 and Nos. 9-12. From the Nos. 1-17 patterns, $\mathbf{X}_R$ is determined.

Detailed analyses are conducted for the 17 cases to obtain $\mathbf{Y}_R$ = (Y_1, Y_2,,,,,, Y_{17}) in Eq. (11). The factors of the analytical sites for the detailed analysis are set to

$(a_{max}, a_{median}, a_{min}) = (428, 126, 10)$ km^3

$(b_{max}, b_{median}, b_{min}) = (77.5, 48.6, 30.3)$ %

$(c_{max}, c_{median}, c_{min}) = (1.2, 0.8, 0.6)$ %

$(d_{max}, d_{median}, d_{min}) = (71.3, 47.0, 27.5)$ %

$(e_{max}, e_{median}, e_{min}) = (502, 268, 73)$ household

$(f_{max}, f_{median}, f_{min}) = (1293, 390, 73)$ persons

$(g_{max}, g_{median}, g_{min}) = (57.7, 49.5, 31.2)$ ha

$(h_{max}, h_{median}, h_{min}) = (68628, 55765, 43315)$ million JPY

$a_{max},..., h_{max}$: maximum values of $a,..., h$.

$a_{median},..., h_{maedian}$: median values of $a,..., h$.

$a_{min},..., h_{min}$: minimum values of $a,..., h$.

The maximum, median, and minimum values of the parameters correspond to the values "1", "0", and "-1" in Table 3-4. The maximum, median, and minimum values are determined from the actual values of Site A, Site B, and Site C.

Table 3-4. $L_{16}(2^{15})$ orthogonal array.

No.	a_s	b_s	c_s	d_s	e_s	f_s	g_s	h_s	Damage cost Y (Million JPY)
1	1	1	1	1	1	1	1	1	3,084
2	1	1	1	1	-1	-1	-1	-1	679
3	1	1	-1	-1	1	1	1	1	23,443
4	1	1	-1	-1	-1	-1	-1	-1	3,029
5	1	-1	1	-1	1	1	-1	-1	7,805
6	1	-1	1	-1	-1	-1	1	1	1,494
7	1	-1	-1	1	1	1	-1	-1	18,717
8	1	-1	-1	1	-1	-1	1	1	3,164
9	1	1	1	-1	1	-1	1	-1	1,063
10	-1	1	1	-1	-1	1	-1	-1	1,429
11	-1	1	-1	1	1	-1	1	-1	2,676
12	-1	1	-1	1	-1	1	-1	1	3,766
13	-1	-1	1	1	1	-1	-1	1	1,496
14	-1	-1	1	1	-1	1	1	-1	826
15	-1	-1	-1	-1	1	-1	-1	1	862
16	-1	-1	-1	-1	-1	1	1	-1	499
17	0	0	0	0	0	0	0	0	9,673

a_s, b_s, c_s, d_s, e_s, f_s, g_s, and h_s: standardized values for a, b, c, d, e, f, g, and h.
Site A: Nos. 5-8 and Nos. 13-16 Site B: No. 17 Site C: Nos. 1-4 and Nos. 9-12.

For example, to obtain damage cost Y_1, the site data are tuned up to (a_{max}, b_{max}, c_{max}, d_{max}, e_{max}, f_{max}, g_{max}, h_{max}) for the geometry of Site C, and for damage cost Y_5, the site data (a_{max}, b_{min}, c_{max}, d_{min}, e_{max}, f_{max}, g_{min}, h_{min}) are assigned for the geometry of Site A. Through the regression analysis, in which the vector of the factors is set to $\mathbf{x}_R = (a_s, b_s, c_s, d_s, e_s, f_s, g_s, h_s)$, the optimum regression coefficient vector, $\hat{\beta}$, which presents the sensitivity, is determined by Eq. (29).

The results of the sensitivity analysis based on the orthogonal array, namely, the absolute values of the regression coefficient, $|\hat{\beta}|$, are shown in Fig. 3-7. Since the factor values are standardized to -1, 0, and 1in the sensitivity analysis, the regression coefficients no longer have a physical meaning. According to the figure, factors *a, c, e,* and *f* show high sensitivity to the damage costs of the earth-fill dams.

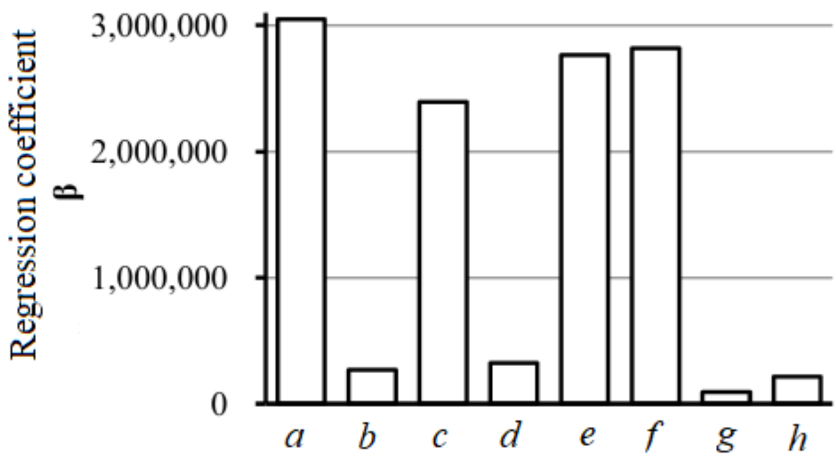

Figure 3-7. Sensitivity of each factor to damage costs.

The principal component analysis is a multivariate analysis method that synthesizes variables called the principal components. The principal components can present the overall variation with a small number of uncorrelated variables from many correlated variables. The principal component analysis is used to clarify how the four selected factors, *a, c, e,* and *f*, are related to the damage costs calculated by the detailed method.

The contribution rate is the ratio of information occupied by the relevant principal component to the total amount of data. The factor loading is calculated as the correlation coefficient of each variable for the principal component. The closer the absolute value of the factor loading is to 1, the higher the correlation. According to the results of the principal component analysis for the 31 earth-fill dams and the result shown in Fig. 3-8, the variables that are closely related to the first principal component are *e*, *f*, and the damage costs, while the variables that are closely related to the second principal component are *a* and *c*. In other words, factors *a* and *c* are the factors giving variability to the predicted damage costs. Although the sensitivities of factors *a* and *c* are high, according to Fig. 3-8, the two factors are related to the second principal component. The reason is that the sensitivity analysis is done based on the three sites, while the principal component analysis is done based on all 31sites, and the great variability in the geometry is added to the principal component analysis. If either *a* or *c* is changed, and another factor is fixed, the changed factor of *a* or *c* has a strong correlation to the damage costs. Therefore, the crossing term for *a* and *c* is considered to determine the response surface. To improve the accuracy of the response surface, alternative factors, ln *a* and ln *c*, are considered for factors *a* and *c* to reduce the effect of the variability in the two factors (Tateishi 2021), respectively.

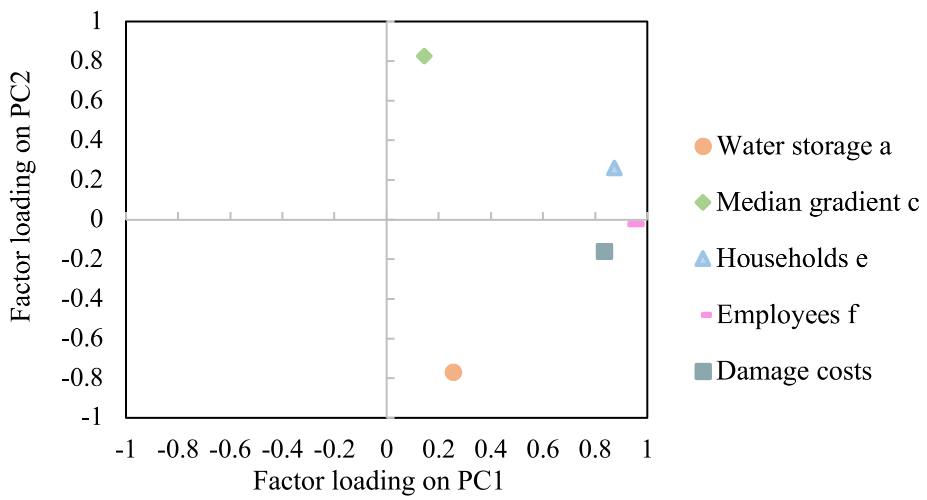

Figure 3-8. Factor loading of each variable using principal component analysis.

For the construction of the model for the probability of overtopping, four variables were chosen that are critical in the calculation of the rainfall hyetograph and storage function method, namely, *CA*: catchment area of the earth-fill dam, *a*: effective water storage of the earth-fill dam, R_e: peak rainfall intensity over the 72-hour period of precipitation during the July 2018 heavy rain, and Q_d: design flow discharge of the earth-fill dam. Due to the varying scales among the variables, it was difficult to fit a model with a better performance in the actual construction of this model. Therefore, all the variables are logarithmical, thus reducing the variable space, which is conducive to an improvement in model accuracy. The histograms of the features before and after performing the logarithmic transformation are provided in Figures 3-9. From the figures, it can be seen that the distribution of data is more uniform after the logarithmic transformation.

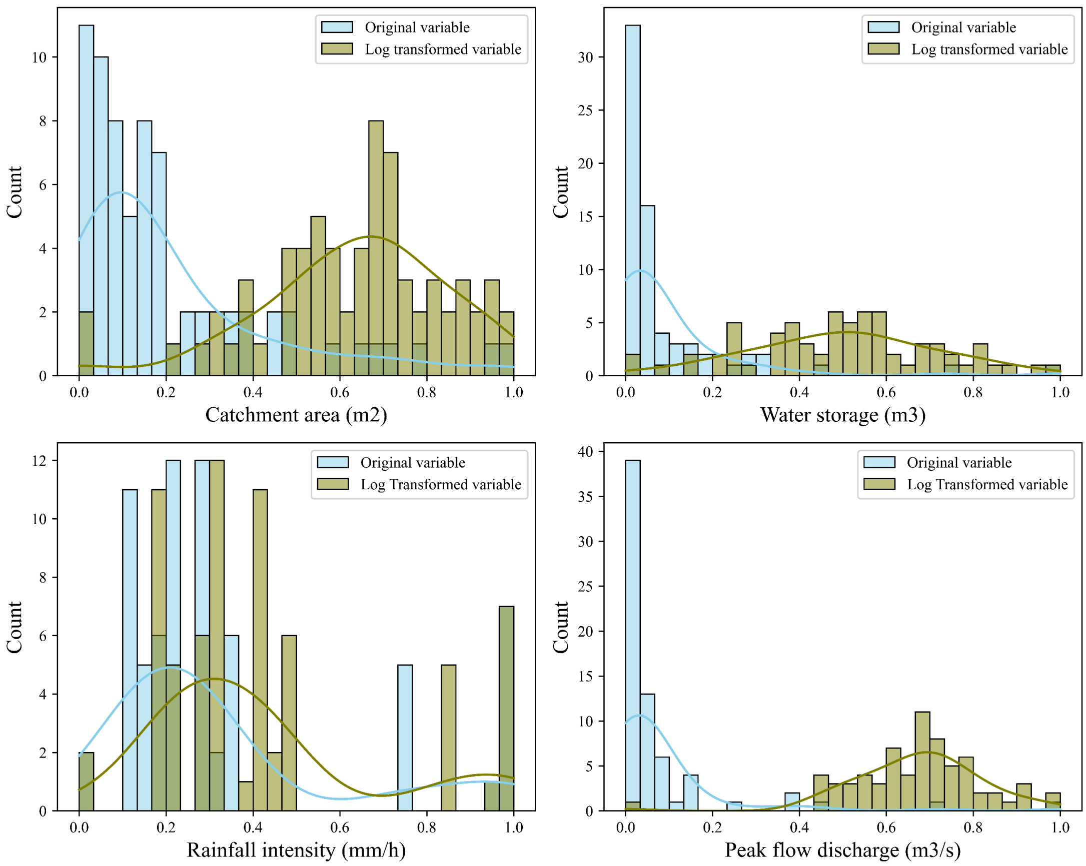

Figure 3-9. Histograms of overtopping probability variables.

3.3 Surrogate models

3.3.1 Response surface method

Outline of response surface method

The response surface method, which is based on the experimental design concept, can be expressed as a regression function, as seen in the following equation:

$$y_R = \beta \mathbf{x}_R + \varepsilon_R \tag{27}$$

where y_R is the response surface, $\mathbf{x}_R^T = (x_{R1}, x_{R2}, \ldots, x_{Rn})$ is the vector of the factor variables, n is the number of factors, $\beta^T = (\beta_1, \beta_2, \ldots, \beta_n)$ is the vector of the regression coefficients, and ε_R is the error term. By substituting several sampled values for $\mathbf{x}_R$, the factor matrix, $\mathbf{X}_R$ ($m \times n$), is constructed. Here, m is the number of analytical cases. The output vector, $\mathbf{Y}_R$ ($m \times 1$), on the other hand, is obtained by the m- cases detailed method. From these values, Eq. (11) is derived.

$$\mathbf{Y}_R = \mathbf{X}_R \beta + \mathbf{E}_R \tag{28}$$

where $\mathbf{E}_R$ ($m \times 1$) is the error term vector. By minimizing $\mathbf{E}_R^T \mathbf{E}_R$, the optimum regression coefficient vector, $\hat{\beta}$, is determined as

$$\hat{\beta} = \left(\mathbf{X}_R^T \mathbf{X}_R\right)^{-1} \mathbf{X}_R^T \mathbf{Y}_R \tag{29}$$

In this study, variable y_R represents the damage costs due to floods, which is the total monetary value of the whole inundation area, and variable $\mathbf{X}_R$ represents the factors related to these damage costs, which are selected through a sensitivity analysis. If detailed flood simulations for sampled factors $\mathbf{X}_R$ are conducted, and corresponding damage costs $\mathbf{Y}_R$ are obtained, regression coefficient vector β is determined. Once coefficient β has been determined, the damage costs can be estimated by means of Eq. (28).

3.3.2 Gaussian Process Regression

The Gaussian process is characterized by a collection of random variables. The joint distribution of any finite number of random variables is the Gaussian distribution. The Gaussian distribution is determined by mean function $m(x)$ and covariance function $k(x,x')$, also referred to as the kernel function (Rasmussen and Williams, 2005). The mean and covariance functions of the posterior distribution can be updated based on prior data points, allowing for the prediction of new data.

The expression for the Gaussian process is shown in Equation (30).

$$f(\boldsymbol{x}) \sim \mathrm{GP}\,(m(\boldsymbol{x}), \mathrm{K}(\boldsymbol{x}, \boldsymbol{x}')) \tag{30}$$

where f refers to the Gaussian process, and input variables $x_{i,j}$ (i∈m, j∈n) form input matrix $\boldsymbol{X}$, shown in Equation (31).

$$\mathbf{X}_{m\times n} = \begin{pmatrix} \boldsymbol{x}_{11} & \cdots & \boldsymbol{x}_{1n} \\ \vdots & \ddots & \vdots \\ \boldsymbol{x}_{m1} & \cdots & \boldsymbol{x}_{mn} \end{pmatrix} \tag{31}$$

$\boldsymbol{X}$ is an $m\times n$ dimensional matrix, for which m represents the number of earth-fill dams selected in this study, and n represents the selected variables that have an impact on the risk assessment of each earth-fill dam, which will be elaborated in Section 3.2 Parameters for surrogate model, and the function $f(\boldsymbol{X})$ refers to damage cost and overtopping probability of earth-fill dams.

In practice, the forms of the surrogate models for the damage cost and overtopping probability are generally assumed as shown in Equation (32). Function $f(\boldsymbol{X})$ is a zero-mean Gaussian process, given by Equation (30), and the statistical distribution of noise is assumed to follow a zero-mean Gaussian distribution.

$$y = f(\boldsymbol{X}) + \varepsilon, \varepsilon \sim N(0, \sigma_n^2 \boldsymbol{I}) \tag{32}$$

For a predicted variable of earth-fill dam $\boldsymbol{X}^*$, the corresponding function f^* can be predicted by constructing a joint distribution with the observations, as follows:

$$\begin{bmatrix} y \\ f^* \end{bmatrix} \sim N(0, \begin{bmatrix} \mathrm{K}(\boldsymbol{X},\boldsymbol{X}) + \sigma_n^2 \boldsymbol{I} & \mathrm{K}(\boldsymbol{X},\boldsymbol{X}^*) \\ \mathrm{K}(\boldsymbol{X}^*,\boldsymbol{X}) & \mathrm{K}(\boldsymbol{X}^*,\boldsymbol{X}^*) \end{bmatrix}) \tag{33}$$

The posterior distribution of function *f**, shown in Equation (33), can be obtained by calculating the joint distribution, whose mean function and covariance function are as given by Equation (34).

$$P(f^* | \boldsymbol{X}, \boldsymbol{X}^*, y) \sim N(\overline{f}^*, \operatorname{cov} f^*) \tag{34}$$

$$\begin{aligned} \overline{f}^* &= \mathrm{K}(\boldsymbol{X}^*,\boldsymbol{X})[\mathrm{K}(\boldsymbol{X},\boldsymbol{X}) + \sigma_n^2 \boldsymbol{I}]^{-1} y \\ \operatorname{cov} f^* &= \mathrm{K}(\boldsymbol{X}^*,\boldsymbol{X}^*) - \mathrm{K}(\boldsymbol{X}^*,\boldsymbol{X})[\mathrm{K}(\boldsymbol{X},\boldsymbol{X})\sigma_n^2 \boldsymbol{I}]^{-1} \mathrm{K}(\boldsymbol{X},\boldsymbol{X}^*) \end{aligned} \tag{35}$$

The choice of the kernel function is crucial for the GPR as it determines the shape and properties of the function space and has a great impact on the accuracy of the model. In this paper, three commonly used kernel functions are selected, namely, the Radial Basis Function (RBF) kernel, Matérn kernel (smoothness parameter $v = 1.5$ and 2.5), and Rational Quadratic Kernel (RQ), which are shown in Equations (36) to (38). Next, three different models are constructed, and the most suitable kernel function is determined by comparing the root mean square error (RMSE).

$$K_{RBF}(x, x') = \exp(-\frac{|d|^2}{2l^2}) \tag{36}$$

$$K_{matern}(x, x') = \frac{2^{1-v}}{\Gamma(v)} (\sqrt{2v}\frac{|d|}{l})^v K_v(\sqrt{2v}\frac{|d|}{l}) \tag{37}$$

$$K_{RQ}(x, x') = (1 + \frac{|d|^2}{2\alpha l})^{-\alpha}, \alpha \ge 0 \tag{38}$$

where l is the length scale, α is the shape parameter of the kernel, and d is the Euclidean distance.

3.3.3 XGBoost

eXtreme Gradient Boosting (XGBoost), proposed by Chen (2016), is a powerful machine learning algorithm based on ensemble learning. It is widely used for classification and regression tasks in various fields.

Ensemble learning is classified into bagging, boosting, and stacking, which combine multiple models to enhance performance and robustness. XGBoost is a type of boosting algorithm, where the best results are obtained by sequentially correcting the errors of the previous weak learner. It features an additive model and employs a stepwise forward strategy, i.e., adding a new model at each step as well as correcting the error of the previous step at each step, so only the residuals of the previous step need to be optimized. The XGBoost algorithm is represented by Equation (39) and shown in Figure 3-10.

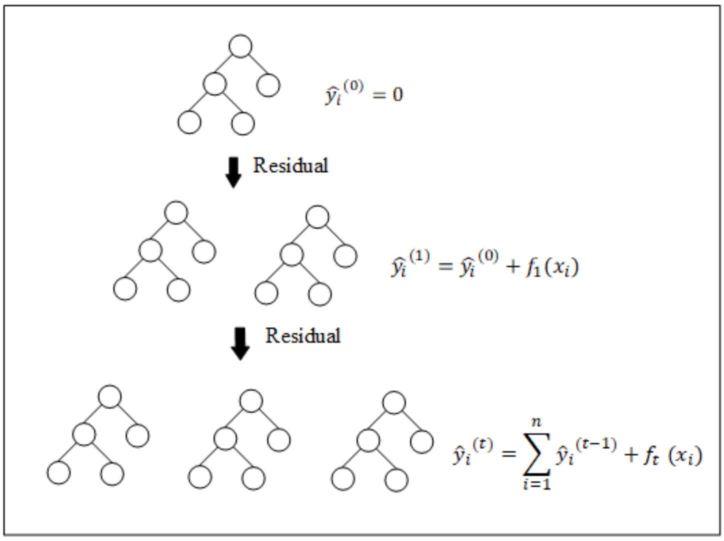

Figure 3-10. Introduction of XGBoost algorithm.

$$\hat{y}_i^{(t)} = \hat{y}_i^{(t-1)} + f_t(x_i) \tag{39}$$

In this paper, it is assumed that the basic learner of XGBoost is the classification and regression tree (CART) model $f(x)$. Assuming that k regression trees are constructed, the XGBoost model can be represented as follows:

$$\hat{y}_i = \sum_{k=1}^{K} f_k(x_i) \tag{40}$$

where $\hat{y}_i$ refers to the predicted damage cost and overtopping probability by XGBoost in this study, x_i means the variables selected to construct the model, K is the total number of trees, $f(x_i) = w_{q(x_i)}$ is the model for each tree, and w denotes the score or weight assigned to each leaf, namely, prediction value $w \in \mathrm{R}^T$. q represents the structure of each tree, $q : \mathrm{R}^m \rightarrow T$. It can be clearly understood from the formula, $f(x_i) = w_{q(x_i)}$, to which leaf each of the i features (variables for damage cost and overtopping probability) belongs as well as the score of each feature.

The XGBoost model optimizes its objective function, comprising a loss function and a regularization term, using a second-order Taylor expansion. This expansion approximates the loss function, allowing for the calculation of first-order and second-order derivatives. By minimizing this approximated function, the model determines optimal leaf weights for each iteration. This process enables efficient tree construction, progressively reducing residuals and enhancing the model's predictive accuracy while maintaining regularization to prevent overfitting.

The XGBoost model incorporates numerous hyperparameters, including maximum tree depth, learning rate, regularization parameters and subsampling rate. Inappropriate selection of these hyperparameters may lead to overfitting, potentially affecting the generalizability of model. Consequently, hyperparameter optimization is crucial for ensuring optimal model performance. This study employed Bayesian optimization (BO) for hyperparameter tuning.

3.4 SHapley Additive exPlanations

SHapley Additive exPlanations (SHAP), proposed by Shapley (1953), was originally applied in game theory as a value for interpreting model outputs. Specifically, it is assumed that each instance in the model has a feature value of a player and assumes that the model's predictions are payouts, with the goal of equitably distributing the contribution of each feature to the model's predictions. The Shapley value is the only attribution method that satisfies the three properties of efficiency, symmetry, and dummy. It guarantees that the difference between the prediction and the average prediction is fairly published between the eigenvalues of the instances (Christoph, 2020), and can provide a good explanatory model for some black-box algorithms, such as XGBoost (Lundberg, 2020).

3.5 Evaluation measures for surrogate model performance

In order to evaluate the performance of the model, evaluation metrics shown in below are used throughout this paper.

3.5.1 Root mean square error

Root mean square error (RMSE) measures the square root of the mean squared difference between the model predictions and the actual observations. Since the error is squared, larger errors are given more weight. The expression of RMSE is given in Equation (41).

$$RMSE = \sqrt{\frac{\sum_{i=1}^{n}(y_i - y_i)^2}{n}} \tag{41}$$

3.5.2 Coefficient of determination

Coefficient of determination R^2 captures the proportion of the dependent variable in model that can be predicted by the independent variables, which is given in Equation (42). The larger the value of R^2, the more explanatory the model is. If the value of R^2

is less than 0, it indicates that the model performs worse than using the mean prediction.

$$R^2 = 1 - \frac{SSE}{SST} \tag{42}$$

SSE means residual sum of squares, SST means total sum of squares.

$$SSE = \sum_i (y_i - y_i)^2 \tag{43}$$

$$SST = \sum_i (y_i - \overline{y})^2 \tag{44}$$

Where y_i is observations, y_i refers to predicted value.

In this paper, we use RMSE and R^2 to evaluate the accuracy of surrogate models. The less the RMSE and bigger the R^2 are, the better the model is.

Reference

Aven, T. (2016). Risk assessment and risk management: Review of recent advances on their foundation. European journal of operational research, 253(1), 1-13.

Chen, T., & Guestrin, C. (2016, August). Xgboost: A scalable tree boosting system. In Proceedings of the 22nd acm sigkdd international conference on knowledge discovery and data mining (pp. 785-794).

Christoph, M. (2020). Interpretable machine learning: A guide for making black box models explainable. Leanpub.

Corominas, J., van Westen, C., Frattini, P., Cascini, L., Malet, J. P., Fotopoulou, S., ... & Smith, J. T. (2014). Recommendations for the quantitative analysis of landslide risk. Bulletin of engineering geology and the environment, 73, 209-263.

Faber, M. H., & Stewart, M. G. (2003). Risk assessment for civil engineering facilities: critical overview and discussion. Reliability engineering & system safety, 80(2), 173-184.

Japan Meteorological Agency (JMA), https://www.jma.go.jp/jma/indexe.html. Accessed in December 21, 2024

Kimura, T. (1967). Storage function method, Public Works Research Institute, Ministry of Construction.

Koutsoyiannis, D. (2004). Statistics of extremes and estimation of extreme rainfall: I. Theoretical investigation/Statistiques de valeurs extrêmes et estimation de précipitations extrêmes: I. Recherche théorique. Hydrological sciences journal, 49(4).

Lundberg, S. M., Erion, G., Chen, H., DeGrave, A., Prutkin, J. M., Nair, B., ... & Lee, S. I. (2020). From local explanations to global understanding with explainable AI for trees. Nature machine intelligence, 2(1), 56-67.

MAFF (Ministry of Agriculture, Forestry and Fisheries). (2015). Land improvement enterprise design guideline "reservoir maintenance" (draft), p. I_159-I_170.

Mizuma, K., et al. (2016). Simplified method for estimating risks due to earth-dam breaches using response surface method. Irrigation, Drainage and Rural Engineering Journal, 84(1), I_47-I_55.

Nishimura, S., Shibata, T. and Shuku, T. (2021). Reliability-based design for earth-fill dams against severe natural disaster events, Soils and Foundations, 6(2), 271-282.

Rasmussen, C. E. (2003). Gaussian processes in machine learning. In Summer school on machine learning (pp. 63-71). Berlin, Heidelberg: Springer Berlin Heidelberg.

Rural Development Bureau, MAFF. (2019). Act on the Management and Conservation of Earth-fill Dams. https://www.maff.go.jp/j/nousin/bousai/bousai_saigai/b_tameike/kanrihozenhou.html

Shapley, L. (1953). A Value for n-Person Games. In: Kuhn, H. and Tucker, A., Eds., Contributions to the Theory of Games II, Princeton University Press, Princeton, 307-317.

Shibata, T., Nishimura, S., Tateishi, T., Kuroda, S., Kato, T., Kuribayashi, K., Tanaya, N. (2021). Case History of Risk Evaluation of Earth-Fill Dams Due to Heavy Rain. International Journal of Geoengineering Case History, 6(4), 85-100.

Tateishi, T. (2021). A study on a simple evaluation of the risk of heavy rain disasters in a reservoir in Hiroshima. Proc of 75th Annual Meeting of Chugoku-Shikoku Branch of JSIDRE, I_61-I_63.

Toro, E.F. (1992). Riemann problems and the WAF method for solving the two-dimensional shallow water equations. Philos. Trans. R. Soc. London, Ser. A, 338, 43-68.

Yoon, T.H., Kan, S.-K. (2004). Finite volume model for two-dimensional shallow water flows on unstructured grids. J. Hydraul. Eng., ASCE.

4. Performance Evaluation of Surrogate Models for Earth-fill Dam Overtopping Risk Assessment

4.1 Risk Assessment for Damage Cost of Earth-Fill Dams by Response Surface Method

In this study, nine response surfaces with different factors and conditions, listed in Table 4-1 are examined. For response surfaces 2 and 5-1, the cross term of *a* and *c* is included in order to consider the relationship between factors *a* and *c.* According to the principal component analysis (PCA), these two factors give variability to the

Table 4-1. Purpose of each response surface.

Response surface	Function type of response surface	Number of factors
1	$x_a a + x_c c + x_e e + x_f f$	4
2	$x_a \ln a + x_c \ln c + x_{ac} \ln a \cdot \ln c + x_e e + x_f f$	5
3-*a*7000	$x_a a + x_c c + x_e e + x_f f$	8
3-*a*11000	$x_a a + x_c c + x_e e + x_f f$	8
4-*a*7000	$x_a \ln a + x_c \ln c + x_{ac} \ln a \cdot \ln c + x_e e + x_f f$	10
4-*a*11000	$x_a \ln a + x_c \ln c + x_{ac} \ln a \cdot \ln c + x_e e + x_f f$	10
5-1	$x_a a + x_c c + x_{ac} a \cdot c + x_e e + x_f f$	5
5-3-*a*-7000	$x_a a + x_c c + x_{ac} a \cdot c + x_e e + x_f f$	10
5-3-*a*11000	$x_a a + x_c c + x_{ac} a \cdot c + x_e e + x_f f$	10

*a*7000: factor *a* is divided by 7000 m^3 into two equations.

*a*11000: factor *a* is divided by 11000 m^3 into two equations.

damage costs. Response surfaces 3-a7000, 3-a11000, 4-a7000, 4-a11000, 5-3-a7000, and 5-3-a11000 are created by setting an arbitrary threshold for the water storage.

In order to evaluate the accuracy of the response surfaces, a method called cross-validation is used in this study.

For 29 earth-fill dams located in Hiroshima and Okayama prefecture, cross-validation is applied. Firstly, after removing one of the 29 earth-fill dams, a regression analysis is performed on the remaining 28 dams. An error $(x_n - y_n)$ can be obtained by reducing the obtained new damage cost, x_n, to damage cost y_n obtained from the detailed method. "n" is the number of removed dams. By repeating this calculation 28 times, the error e_{rr},($e_{rr} = \sqrt{\sum_{n=1}^{28}(x_i - y_i)^2}$) of the response surface is determined. The response surface with the minimum e_{rr} is determined as the most appropriate one.

From the result, response surface 4-a11000 is the optimum one based on the results of the cross-validation. The response formula is displayed below.

$$\text{Damage cost} = \begin{cases} -1.04\times10^{6}\ln a - 5.02\times10^{7}\ln c + 5.64\times10^{6}\ln a\cdot\ln c \\ +1.67\times10^{3}e + 1.07\times10^{4} f \qquad (a < 11000) \\ \\ -7.30\times10^{4}\ln a - 2.33\times10^{7}\ln c + 2.01\times10^{6}\ln a\cdot\ln c \\ -6.29\times10^{2}e + 4.29\times10^{3} f \qquad (a \geq 11000) \end{cases} \tag{45}$$

Comparisons of the predicted damage costs between the detailed method and the response surface method are shown in Fig. 4.1. According to Fig. 4.1, there is a

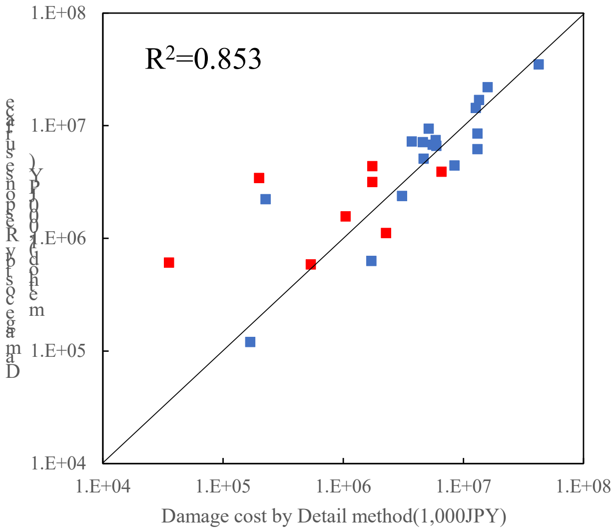

Figure 4-1. Comparison of response surface method and detailed method in damage cost.

significant difference between the response surface method and the detailed method in terms of the small damage costs. The red markers represent the earth-fill dams situated in Hiroshima; the blue markers represent the dams in Okayama. In contrast, the two methods are relatively coincidental in terms of the large damage costs.

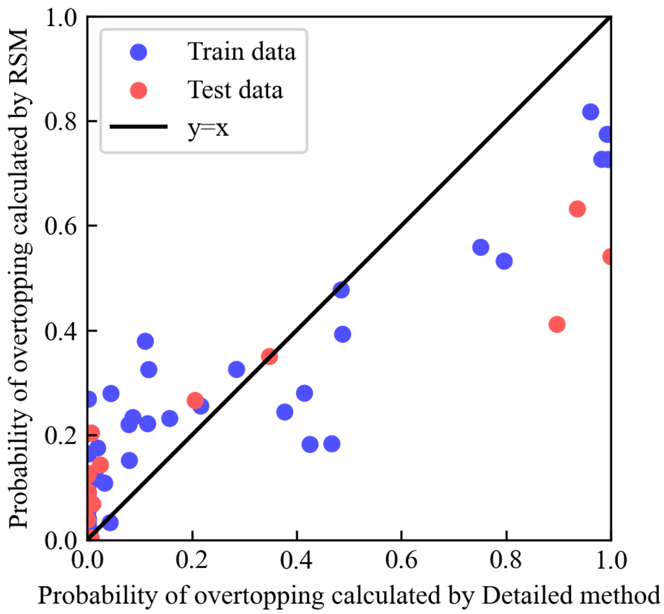

Figure 4-2. Comparison of response surface method and detailed method in overtopping probability.

Subsequently, we constructed response equations using linear regression with the influential factors A, V, Q_d, and R_e, including their interaction terms.

$$P_f = 0.26 + 2.00 \times lna - 0.24 \times lnv + 0.32 \times lnRe - 1.26 \times lnQd - 1.14 \times lna \cdot lnQd \quad (46)$$

The data were divided into training and test sets, and the optimal response equation was selected based on the coefficient of determination (R^2) and Root Mean Square Error (RMSE) of the test set. The performance metrics showed an R^2 value of 0.68 and an RMSE of 0.214. The final prediction results are shown in the Figure 4-2.

4.2 Quantitative Risk Assessment for Overtopping of Earth-Fill Dams by Machine Learning

4.2.1 Model construction

When fitting the two models, the raw data on the 70 earth-fill dams were divided into the same training and test sets for both the GPR model and the XGBoost algorithm at a ratio of 7:3 to ensure that no other factors would influence the comparison of the performance of the two models. As the variables do not have the same units as the predicted values, the data were normalised using z-score normalisation to ensure that all the data would lie on the same scale.

In this case, since there will inevitably be noise in the observation data, a noise term, namely, a white kernel, was additionally added to the function when making the GPR predictions, to improve the performance of the model. On the other hand, there was no need to add an additional noise term to XGBoost since it contains internal mechanisms that can deal with noise. It models the data based on a decision tree model.

To fit the GPR model, four kernel functions were chosen, namely, the RBF kernel, Matern3/2 kernel, Matern5/2 kernel, and Rational Quadratic kernel (as introduced in Section 3.2), and the hyperparameters of each kernel function were optimised using the maximum log marginal likelihood method. The appropriate kernel function was chosen according to the one that had the best performance in terms of the RMSE for the prediction of the test set. Since GPR is an interval estimation, 95% confidence intervals (CI) were also taken into account in the predicted results.

For the construction of the XGBoost model, a decision tree was chosen as the base learner, and the L1 regular term was chosen to prevent overfitting. The XGBoost model has many hyperparameters, which have a great impact on the performance of the model, so the selection of the hyperparameters is particularly important. The set of hyperparameters used in this study are shown in Table 4-2, and Bayesian optimization (BO) was chosen to search the hyperparameter set. To further prevent model overfitting, an early stopping parameter was also designated for the model fitting.

Table 4-2. Hyperparameters in XGBoost.

Hyperparameter	Range	Data type
Subsample	[0.5,1.0]	Uniform
Max depth	[3,10]	Integer
Learning rate α	[-6,0]	Log uniform
Regulation λ	[-6,0]	Log uniform
Gamma γ	[-6,0]	Log uniform

Subsample: ratio sampled from training set during each boosting iteration.

Learning rate α: step size shrinkage for feature weights.

Max depth: maximum depth of each CART model.

Regulation: L1 regulation (Lasso) term on weights.

Gamma: minimum loss reduction for further leaf node partitioning.

4.2.2 Model validation

Table 4-3. Performance metrics of models

	Damage cost		P_f of overtopping	
	GPR	XGBoost	GPR	XGBoost
RMSE	0.077	0.048	0.107	0.084
R^2	0.853	0.941	0.836	0.897

Note: metrics RMSE and R^2 are both calculated by test set.

For the surrogate model of the damage cost, the results of the prediction of the training and test sets, using the fitted models, are provided in Figure 4-3. The

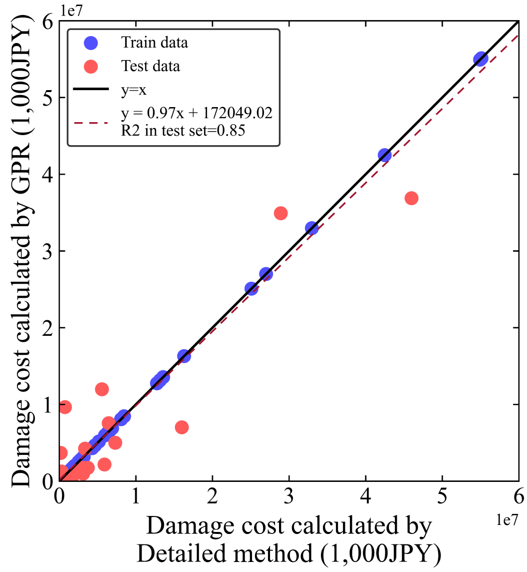

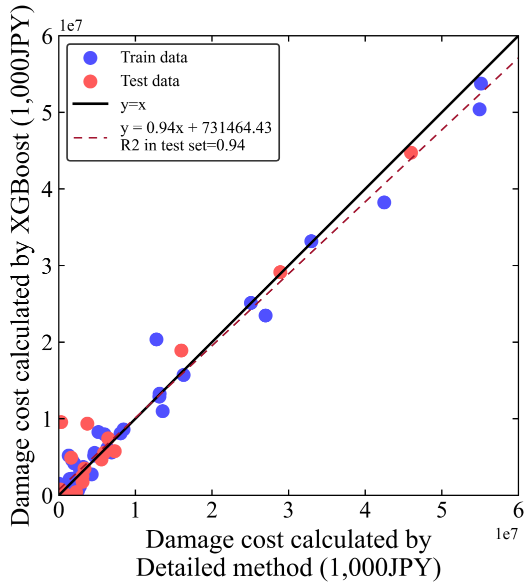

Figure 4-3. Comparisons of damage costs by GPR and XGBoost.

performance of the two models is summarised in Table 4-3. In the GPR model, the RMSE is 0.077, coefficient of determination is 0.853, and the appropriate kernel is determined as the Matérn kernel, v=2.5, while in the XGBoost model, the RMSE is 0.048 and the coefficient of determination is 0.941. As can be seen, the performance of the XGBoost model is better than that of the GPR model.

Based on the XGBoost model, the interpretable method SHAP was applied to calculate the extent to which each feature value contributes to the damage cost by the average value of change in the damage cost as the feature changes. As shown in Figure 4-4, the feature that most contributed to the damage cost is water storage. This is because, as the water storage increases, so does the damage cost. On the other hand, the number of households and number of employees have a positive effect on the damage cost, while the median slope has a negative effect.

For the surrogate model of overtopping probability, the results of the prediction of the test set by the models fitted by the two methods are shown in Table 4-3. Among them, the RMSE and R^2 of the GPR model are 0.107 and 0.836, respectively. The GPR model used the appropriate Matérn kernel of v=1.5, while the XGBoost model used RMSE and R^2 of 0.084 and 0.897, respectively. This suggests that, while both have better generalisation properties, the XGBoost model shows a better performance than the GPR model. The two models are compared in Figures 4-5; the training and test sets are presented separately.

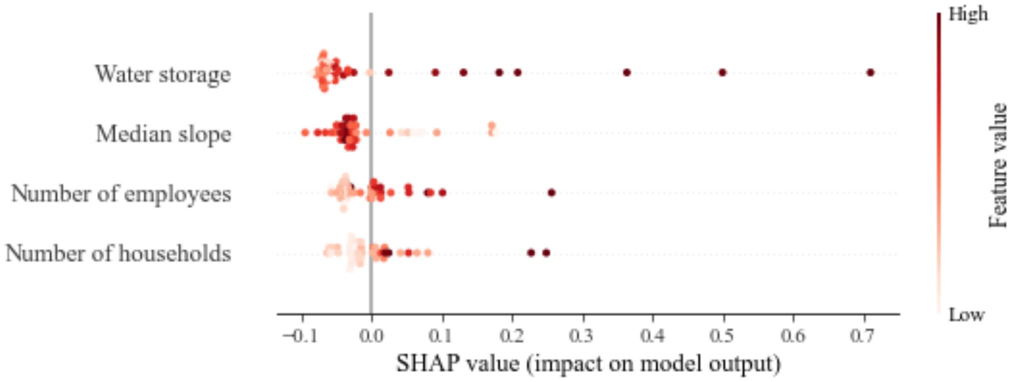

Figure 4-4. SHAP value of damage cost.

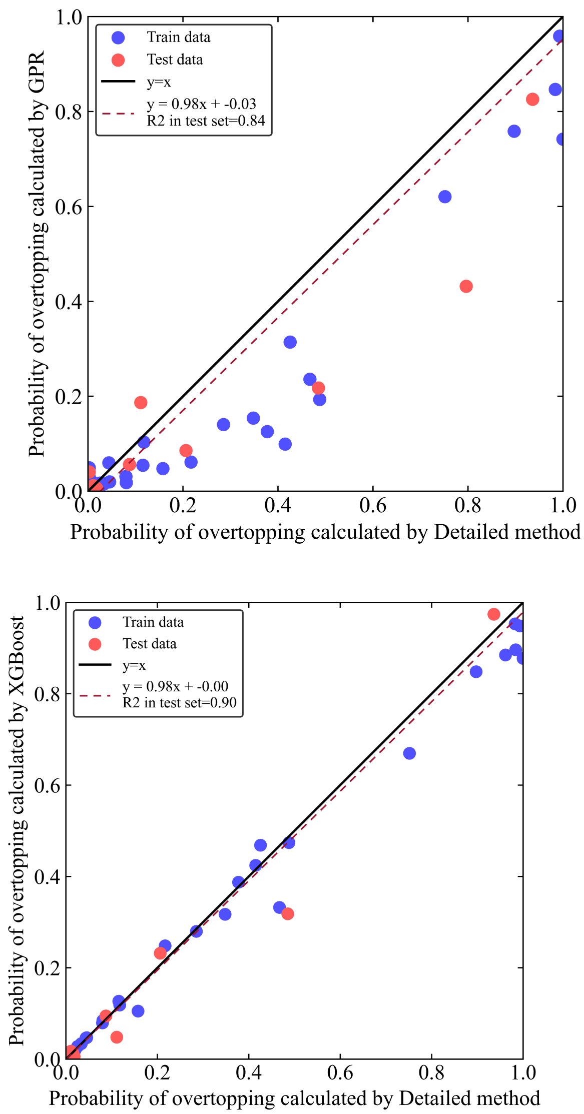

Figure 4-5. Comparisons of overtopping probability by GPR and XGBoost.

Subsequently, the SHAP value is similarly used in the model to explain the extent to which each feature contributes to the probability of overtopping. The results are shown in Figure 4-6. Although the catchment area and water storage have a positive effect on the overtopping probability, the design flow discharge has a strong negative effect on the overtopping probability. Since the design flow discharge is the threshold for determining whether overtopping has occurred or not, we believe that the SHAP values generate reliable common-sense results.

Figure 4-6. SHAP values of overtopping probability.

4.2.3 Risk quantification

In this section, the risk to each earth-fill dam is determined by the damage cost and probability of overtopping which were separately calculated by the detailed method of assessment, the GPR method, and the XGBoost algorithm. Coefficient of determination R^2 was also calculated using entire dataset.

From the results, the R^2 of GPR is 0.921 and the R^2 of XGBoost is 0.994. Therefore, by comparing the indicators, it can be concluded that the XGBoost model is better than the GPR model in terms of making predictions. Boxplot and density plot distributions for the risk calculated using the three models are provided below.

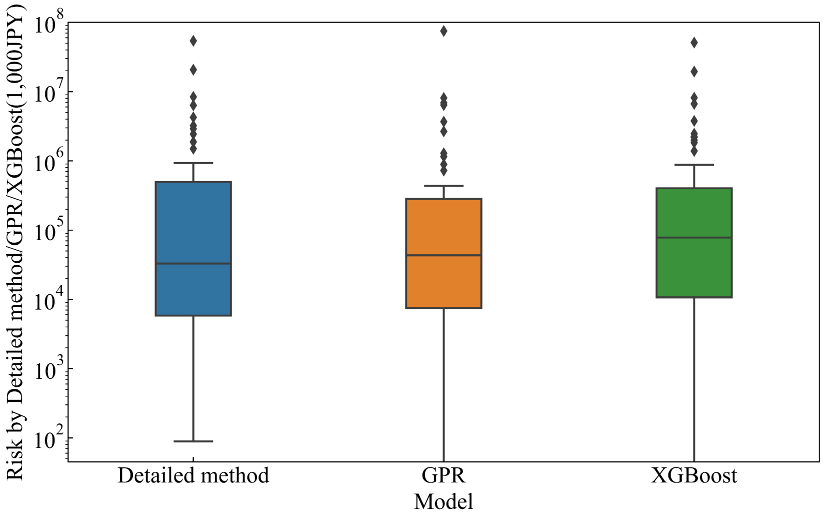

Figure 4-7. Boxplots of risk by detailed method, GPR, and XGBoost.

The boxplots describe the distribution characteristics of data, such as quartiles, median, and outliers. By comparing the boxplots of the data from the detailed method, GPR method, and XGBoost method, the similarities and differences in the distributions of the three methods can be intuitively perceived. From Figure 4-7, it is seen that the predicted values of the GPR model are generally small, and that the quartiles and distributions of the XGBoost model are closer to those of the detailed method.

Quantifying the risk of earth-fill dam overtopping during heavy rainfall events is crucial for flood risk management and disaster prevention. A higher risk ranking indicates a greater potential of risk to downstream areas during such conditions. Figures 4-8 (a) to (b) present comparisons of the risk rankings for GPR and XGBoost by density plots, employing a colour gradient to visualize the density distribution of the data points, with red indicating areas of high density and blue indicating areas of low density. Due to the large magnitude of the risk values, a logarithmic scale was used for the visualisation to enhance the visibility of the differences between the two models. It is evident that both methods achieve high metrics in terms of the evaluations of risks. The results of GPR are more dispersed in the assessment of the risk ranking than those of XGBoost, and both algorithms perform effectively for earth-fill dams with higher risk rankings.

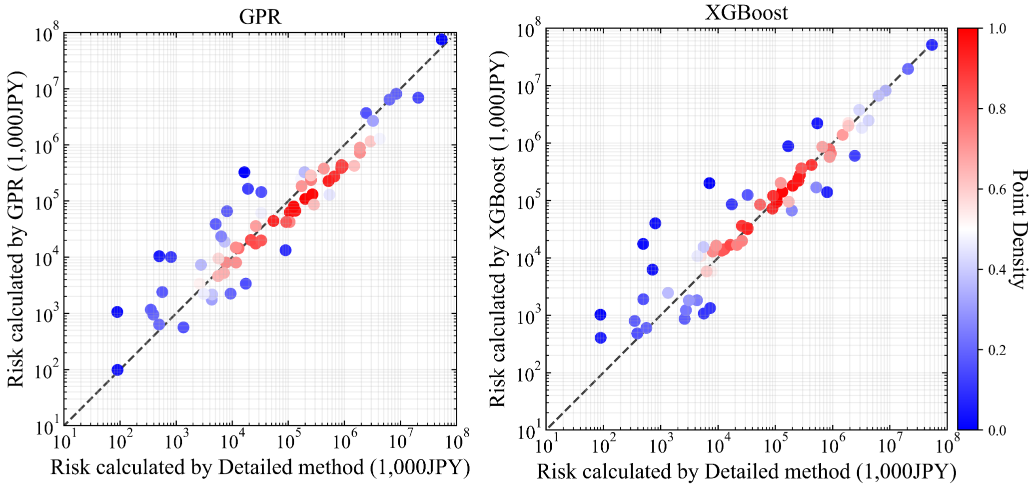

(a) Risk

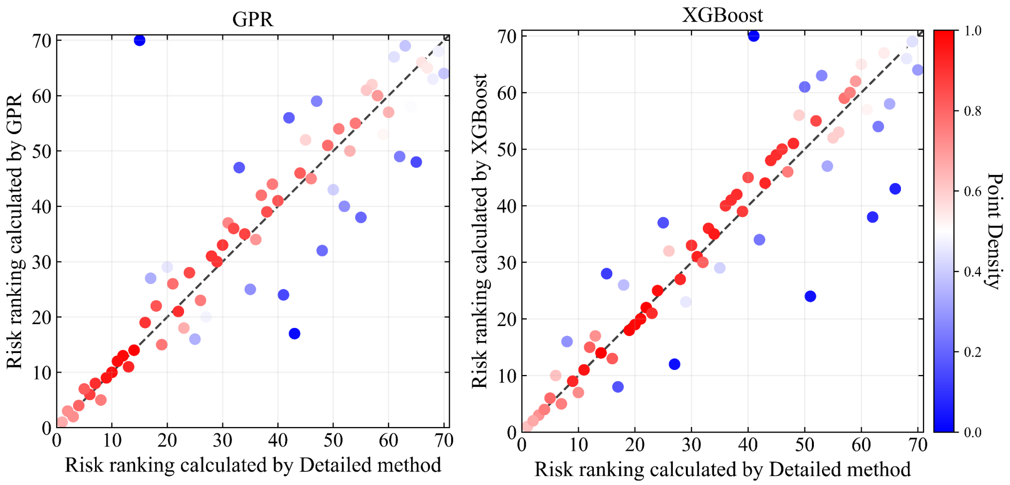

(b) Risk ranking

Figure 4-8. Comparisons of risk and risk ranking by GPR and XGBoost.

Chapter 5 Discussion

5.1 Risk analysis of contributing variables

To further explore the degree of influence of various variables on risk, the risk rankings were subsequently categorized into high (risk ranking 1-23), moderate (risk ranking 24-46), and low (risk ranking 47-70) risks using the natural breaks method. Concurrently, the variables (CA, C, F, E, A, R_e and Q_d) were similarly discretized into three categories to explore the impact of each variable within each risk level. The classifications of the variables are shown in Table 5-1. Given that XGBoost demonstrated a superior performance in both the damage cost and overtopping probability models compared to GPR, the risk calculated by XGBoost will be discussed in the following sections.

Table 5-1. Variable classifications based on natural breaks method.

Variable	Class 1	Class 2	Class 3
Catchment Area (CA, m²)	[0.01, 0.27]	[0.28, 0.71]	[0.74, 3.80]
Water Storage (A, m³)	[1,000, 14,000]	[15,000, 50,000]	[51,000, 811,000]
Slope (C)	[0.0, 1.0]	[1.2, 2.0]	[2.1, 13.6]
Household Density (E, households/km²)	[73.26, 787.72]	[805.13, 1,423.56]	[1,440.70, 5,245.53]
Employee Density (F, employees/km²)	[28.78, 668.43]	[730.75,1,303.08]	[1,306.01, 3,482.55]
Rainfall Intensity (R_e, mm/h)	[18.0, 24.0]	[25.0, 28.0]	[29.0, 52.5]
Design Flow Discharge (Q_d, m³/s)	[0.001, 0.942]	[0.990, 3.000]	[3.040, 68.870]

The rose diagrams are combined with the histograms shown in Figures 5-1 (a) to (c) and provide a comprehensive visualization of the frequency distribution of different variable categories across the three risk levels. This representation allows for the interpretation of how each variable contributes to the overall risk assessment. The low-risk level earth-fill dams (Figure 5-1 (a)) are characterized by a larger design flow discharge, steeper slopes, and fewer employees in the downstream area. They typically have fewer households, smaller catchment areas, lower water storage capacities, and lower peak rainfall intensities (predominantly Class 1 and Class 2). Notably, the majority of low-risk earth-fill dams fall into Class 3 for design flow discharge. The moderate-risk level earth-fill dams (Figure 5-1 (b)) show more complex distributions of variable classes and tendencies towards extremes, in other words, a combination of both low and high values for most variables, rather than consistently moderate conditions. The high-risk level earth-fill dams (Figure 5-1 (c)) are mainly characterized by an extremely small design flow discharge, larger

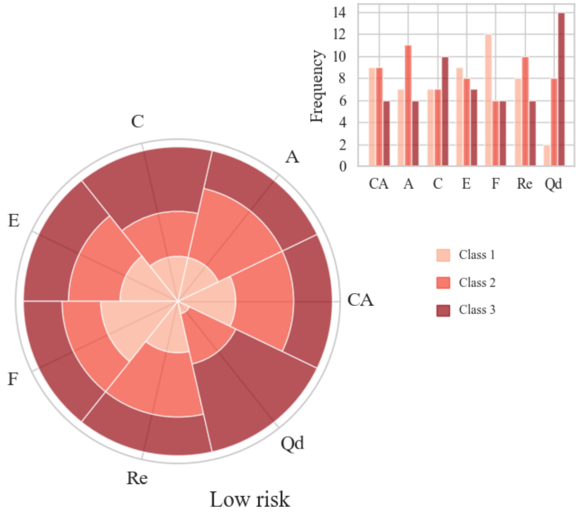

(a) Low risk

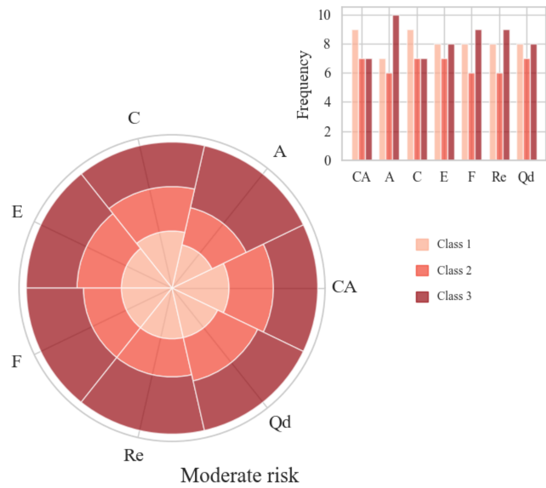

(b) Moderate risk

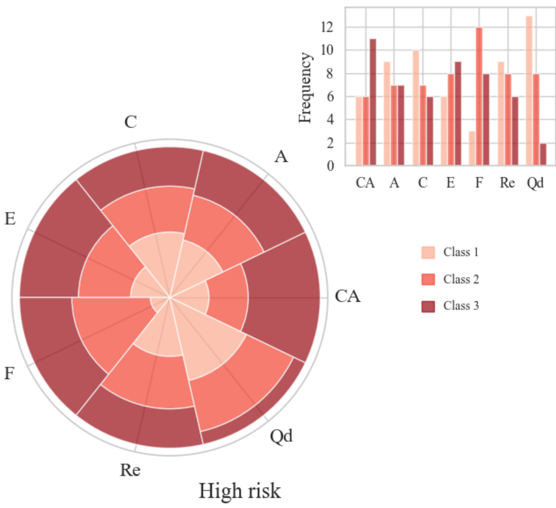

(c) High risk

Figure 5-1. Assessment of variable influence to different risk levels.

downstream area. They also tend to have lower water storage capacities and gentler slopes.

In conclusion, the design flow discharge emerges as the primary determinant of the overtopping risk during heavy rainfall, with a higher discharge capacity correlating strongly with improved dam safety. The influence of other variables is generally in line with the SHAP value trends presented in Figures 4-4 and 4-6.

5.2 Feasibility and implication of risk assessment

This study demonstrates the feasibility of applying machine learning algorithms to assessments of the risk of earth-fill dams due to an overtopping risk assessment. By constructing separate models for damage cost and overtopping probability, coupled with the SHAP value, the machine learning algorithm showcases substantial advantages over traditional methods in terms of time efficiency and high accuracy, while providing insights into the influence of variables on these two critical components of risk quantification. In order to evaluate the risk, the damage costs and probability of overtopping need to be calculated. Neither the damage costs, consisting of the predicted inundation area, land-use and topographical data, and economical information, nor the probability of overtopping, calculated based on a statistical model of the rainfall, characteristics of the catchment area, and ability of the spillway, can be presented simply by a physical model due to the complexity of the high nonlinearity between the factors. The detailed method, used to evaluate the risks, includes these complicated procedures. The surrogate models proposed in this study, based on GPR and the XGBoost, can overcome the disadvantages of the detailed method. Consequently, the proposed approach can make the procedure of the risk evaluation very efficient, and it can be considered a new innovation.

By utilizing data from 70 dams across Okayama and Hiroshima prefectures, the study has developed a robust local risk model that captures regional specificities and provides an intuitive assessment through risk ranking, which significantly enhances the effectiveness of risk management. The categorization of dams into three risk levels, accompanied by a detailed analysis of influencing variables within each category, offers a granular understanding of risk. From the results in Section 4.2.2, the design flow discharge emerged as the most influential variable in a risk assessment, showing a significant negative correlation with risk, while the earth-fill dams characterized with larger catchment areas, gentler slopes, and higher population densities in downstream areas showed elevated risk levels. Therefore, in order to mitigate the risk of overtopping, the real-time monitoring of earth-fill dams with lower design discharge levels and larger catchment areas should be prioritized, while concurrently implementing rapid population evacuation protocols in high-density downstream areas.

5.3 Limitation and future work

This study addresses dam breaches due to overtopping, focusing primarily on rainfall and spillway capacity as critical failure determinants. While other failure modes such as shear failure and piping exist, overtopping remains the predominant cause of breaching (Nishimura et al., 2021). The analysis incorporates several simplifying assumptions that introduce uncertainties. These include the use of fixed hyetograph from the July 2018 heavy rainfall event (Nishimura, S. 2020), which, while representing a significant historical event that caused severe damage throughout Western Japan, may not capture the full variability of potential rainfall patterns.
The analytical results contain inherent uncertainties stemming from multiple sources: the resolution of flood analysis, land use data granularity, and spatial distribution of

economic information (such as household and employee numbers). The response surface methodology, while efficient, introduces additional uncertainty through its approximation of the detailed method. However, the risk ranking maintains reliability as it focuses on relative risk ordering rather than absolute quantities. The failure criteria equations (Eq. 16 and 22) employ safety-side assumptions, not considering reservoir storage effects and using design overtopping heads smaller than actual spillway heights. Previous validation shows that Eq. 16 successfully simulated actual dam breaches during historical rainfall events (Fujii, H. 1991). Since only two regions (Hiroshima and Okayama) were selected for this study, the model's applicability to other regions is currently limited.

A significant limitation is the focus on individual dam failures. While most small earth-fill dams in the study area have independent catchment areas, some are constructed in upstream-downstream arrangements, necessitating consideration of inter-dam interactions. Future research should develop more comprehensive risk models incorporating dam interdependencies within watersheds, including cascading effects (Zhou et al., 2020; Wang et al., 2022; Yang et al., 2022) and hazard chains (Fuchs et al., 2015; Zhang, L. M., & Zhang, S., 2017). These models should account for complex multi-dam and multi-hazard interactions, including amplification and overlapping effects (Zhang et al., 2023).

The current approach of using extreme rainfall events for overtopping probability calculations, while conservative, may lead to risk overestimation. Additionally, relying on historical return periods may not adequately reflect the increasing frequency of extreme weather events due to climate change. Future work should explore more comprehensive approaches to improve extreme rainfall estimations and predictions (Wang et al., 2024), integrate actual water levels rather than assuming full capacity, and incorporate spatial-temporal rainfall data. This could enable the development of more realistic risk assessments and real-time warning models (Pianforini et al., 2024). The proposed methodology will be extended to approximately 4,000 earth-fill dam sites, with continued validation against future heavy rainfall events to assess and improve model accuracy.

Reference

Fuchs, S., Keiler, M., & Zischg, A. (2015). A spatiotemporal multi-hazard exposure assessment based on property data. Natural Hazards and Earth System Science, 15(9), 2127-2142.

Fujii, H., Shimada, K. and Nishimura, S. (1991). Damages of earth-fill dams in Okayama Prefecture due to 1990 Typhoon, Investigation and Research Report for Damages due to Wind and Flood by 1990. 19th Typhoon, Report of Grant-in-Aid for Scientific Research (No. 02306015), pp. 101-130.

Nishimura, S., Shibata, T. and Shuku, T. (2021). Reliability-based design for earth-fill dams against severe natural disaster events, Soils and Foundations, 6(2), 271-282.

Nishimura, S., Takeshita, Y., Nishiyama, S., Suzuki, S., Shibata, T., Shuku, T., ... & Kim, B. (2020). Disaster report of 2018 July heavy rain for geo-structures and slopes in Okayama. Soils and Foundations, 60(1), 300-314.

Pianforini, M., Dazzi, S., Pilzer, A., & Vacondio, R. (2024). Real-time flood maps forecasting for dam-break scenarios with a transformer-based deep learning model. Journal of Hydrology, 635, 131169.

Wang, T., Li, Z., Ge, W., Zhang, Y., Jiao, Y., Sun, H., & Zhang, H. (2022). Calculation of dam risk probability of cascade reservoirs considering risk transmission and superposition. Journal of Hydrology, 609, 127768.

Wang, Z., Wilby, R. L., & Yu, D. (2024). Spatial and temporal scaling of extreme rainfall in the United Kingdom. International Journal of Climatology, 44(1), 286-304.

Yang, J., Shi, Z., Peng, M., Zheng, H., Soares-Frazão, S., Zhou, J., Shen, D., & Zhang, L. (2022). Quantitative risk assessment of two successive landslide dams in 2018 in the Jinsha River, China. Engineering Geology, 304, 106676.

Zhang, L. M., & Zhang, S. (2017). Approaches to multi-hazard landslide risk assessment. In Geotechnical safety and reliability (pp. 312-323).

Zhang, S., Wang, B., Zhang, L., Lacasse, S., Nadim, F., & Chen, Y. (2023). Increased human risk caused by cascading hazards–A framework. Science of the total environment, 857, 159308.

Zhou, X., Chen, Z., Zhou, J., Guo, X., Du, X., & Zhang, Q. (2020). A quantitative risk analysis model for cascade reservoirs overtopping: principle and application. Natural Hazards, 104, 249-277.

Chapter 6 CONCLUSION

This study employed two non-parametric algorithms, GPR and XGBoost and Response surface method, to construct surrogate models for determining the overtopping probability and damage cost, respectively, in order to achieve the risk quantification of earth-fill dams. Based on the 70 dams located in Okayama and Hiroshima prefectures in Japan, the study established a local risk model. The detailed method involves a great deal of effort to evaluate the risks, because land-use data and a flood analysis are required to determine the damage cost, and a statistical model of the rainfall data and an overflow analysis are required to evaluate the probability of overtopping. By constructing a surrogate model using 70 earth-fill dams, it can be applied to the rapid risk assessment of thousands of earth-fill dams in the province. On the other hand, the surrogate model requires four parameters to obtain the damage cost and another four parameters to evaluate the probability of overtopping, with one parameter in common (thus, seven unique parameters), as presented in Section 3.2. Since the effort needed to determine all the parameters for the surrogate model is much lower than that needed for the detailed model, the surrogate model provides greater efficiency. An analysis of the constructed XGBoost model, employed to calculate the SHAP values, found that water storage is the variable that contributes the most to the damage cost model and has a positive impact on the model, whereas the design flow discharge is the variable that contributes the most to the overtopping probability model and has a negative impact on the overtopping probability model, which is in line with our original beliefs.

There are so many earth-fill dams in Japan, and many of them have deteriorated and should be renovated for the sake of safety. Although the demand for dam renovation work is rapidly increasing, the budgets of local governments are insufficient. In the case of Okayama prefecture, the planning of renovations for a very small number (2-3) of earth-fill dams is determined each year. Since it would be impossible to renovate all the deteriorated dams, optimum renovation planning is required. For this purpose, the priority of the earth-fill dams in terms of this renovation work is a key point. The risk ranking is the most rational factor for this priority. Furthermore, the risks were categorised into different levels according to risk ranking and, by exploring the impact of variables at different risk levels, it was found that the design flow discharge of earth-fill dams has the greatest influence on the risks. The XGBoost algorithm not only improves the accuracy of risk assessments, but also provides more scientific support for earth-fill dam repair and maintenance in Japan.

Appendix

The flooding areas of 70 earth-fill dams simulated by finite volume method are partly shown in Figure A-1.

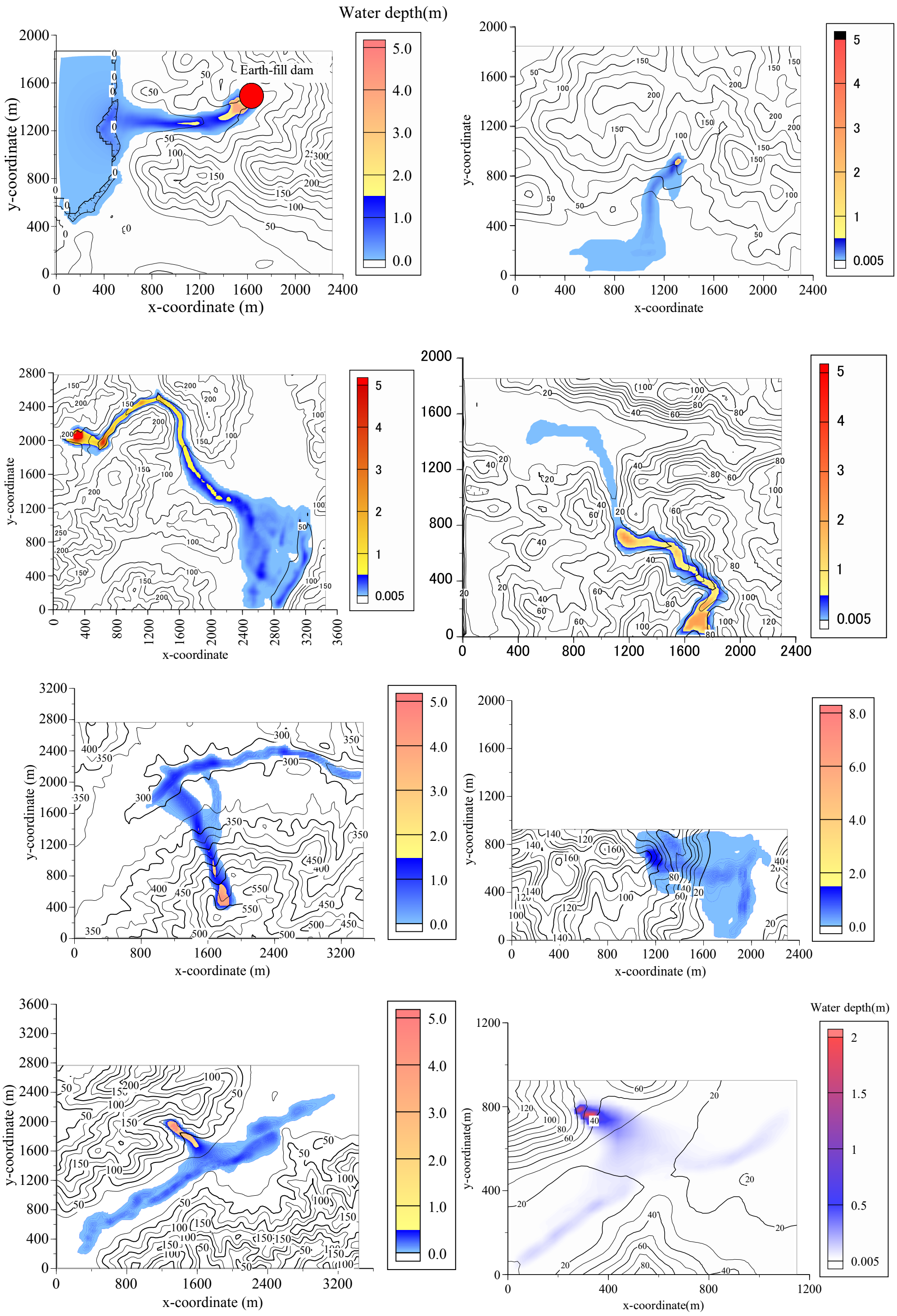

Figure A-1. Results of flooding area (Part1).

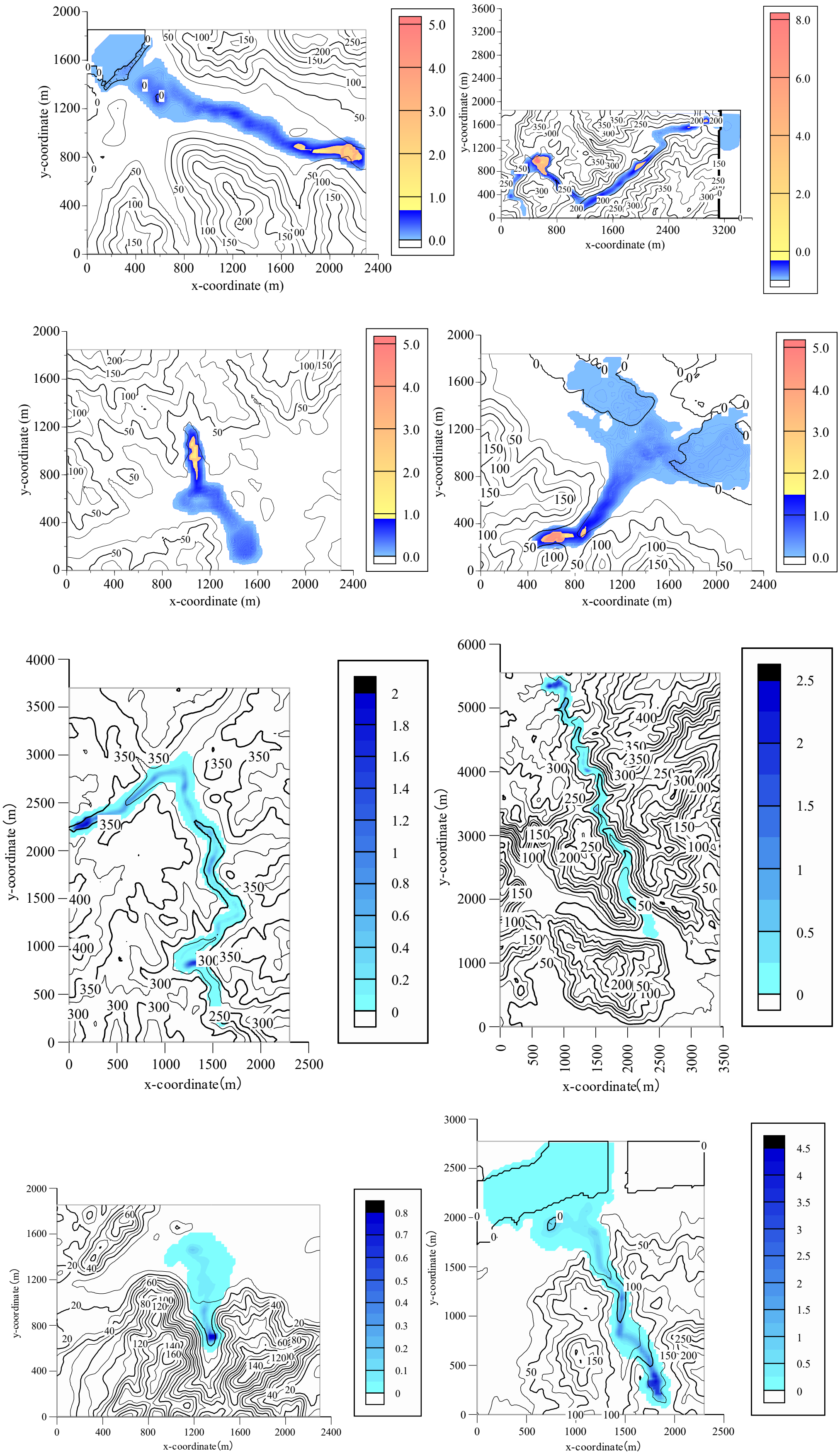

Figure A-1. Results of flooding area (Part2).

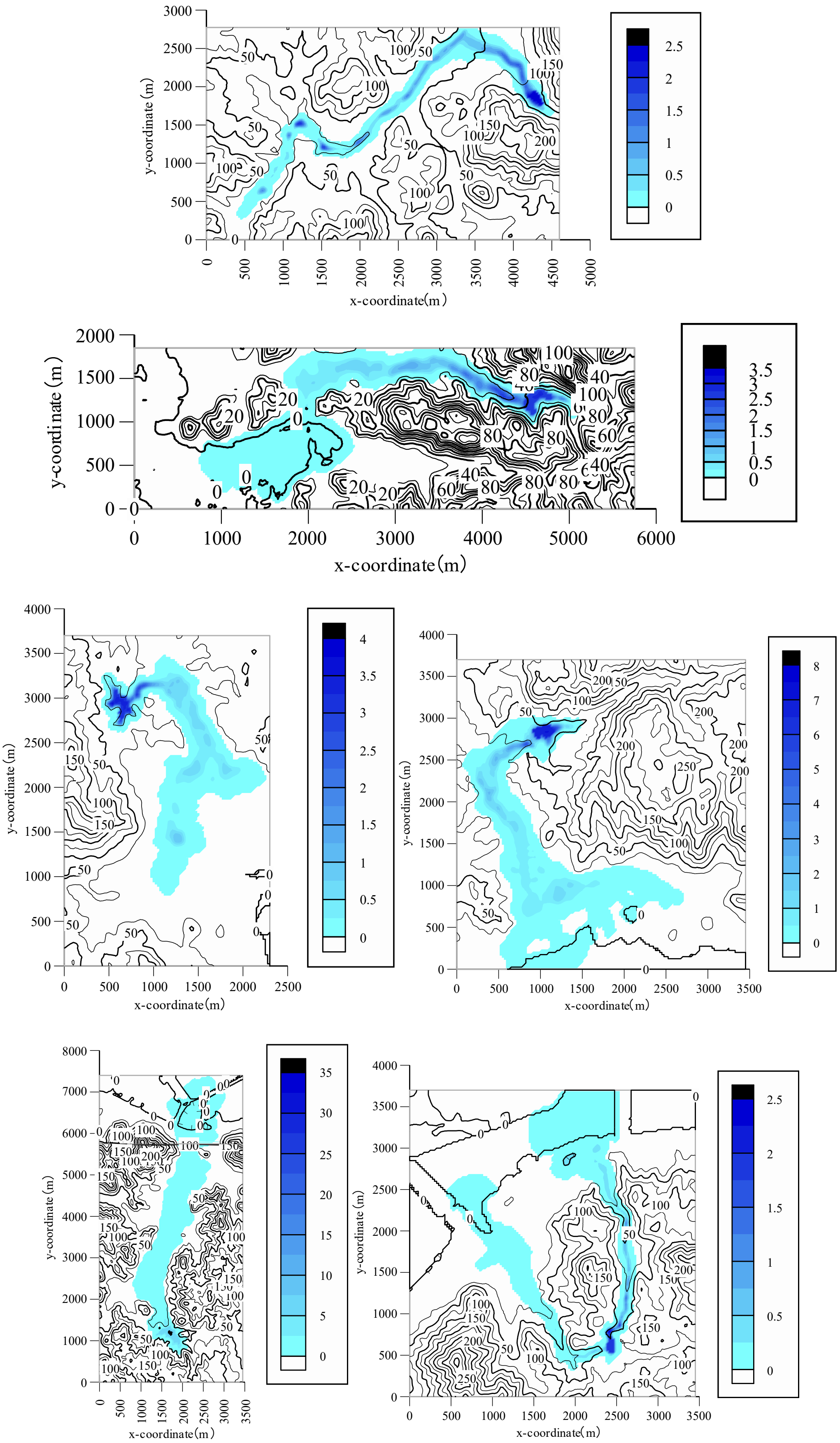

Figure A-1. Results of flooding area (Part3).

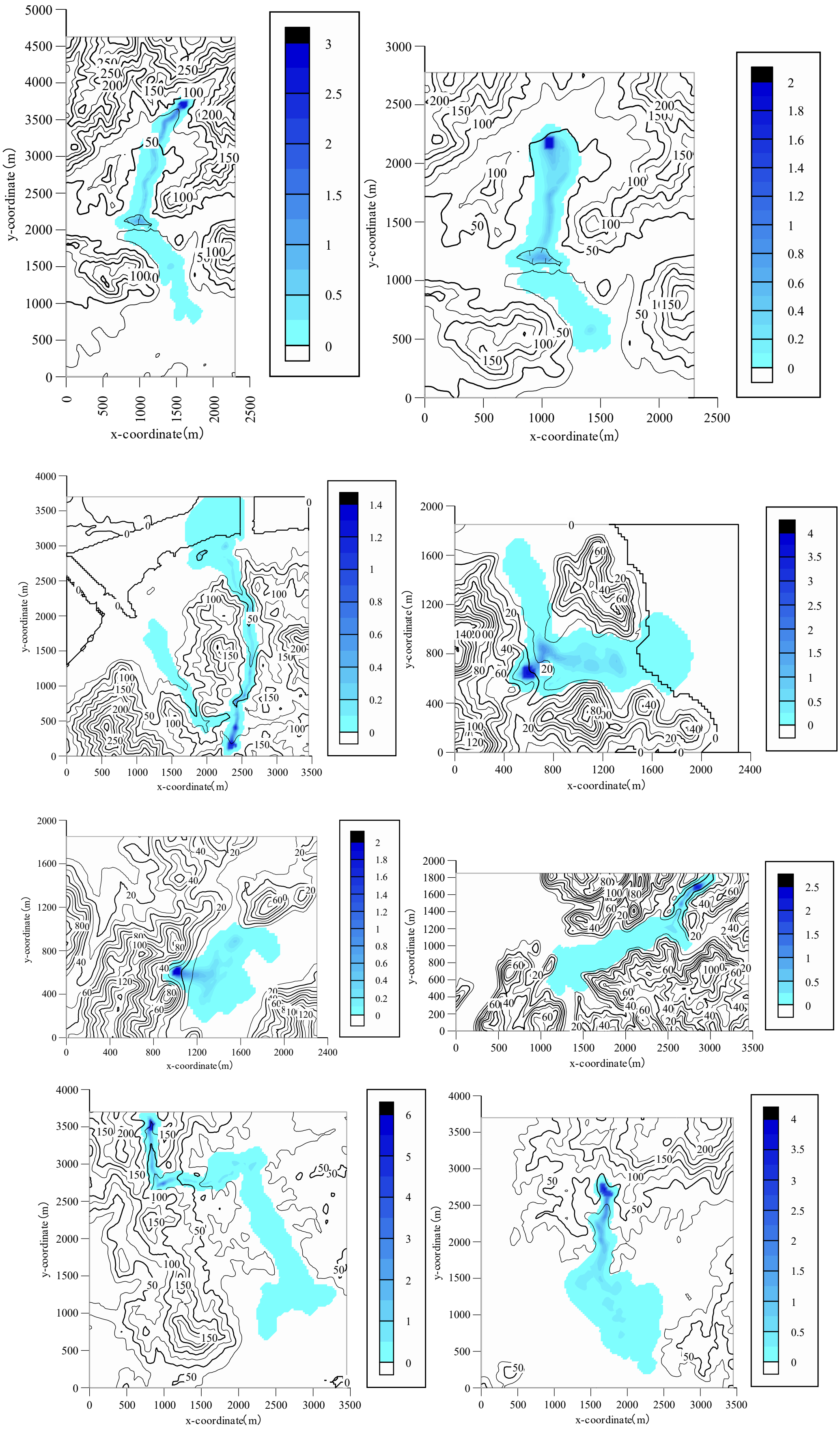

Figure A-1. Results of flooding area (Part4).

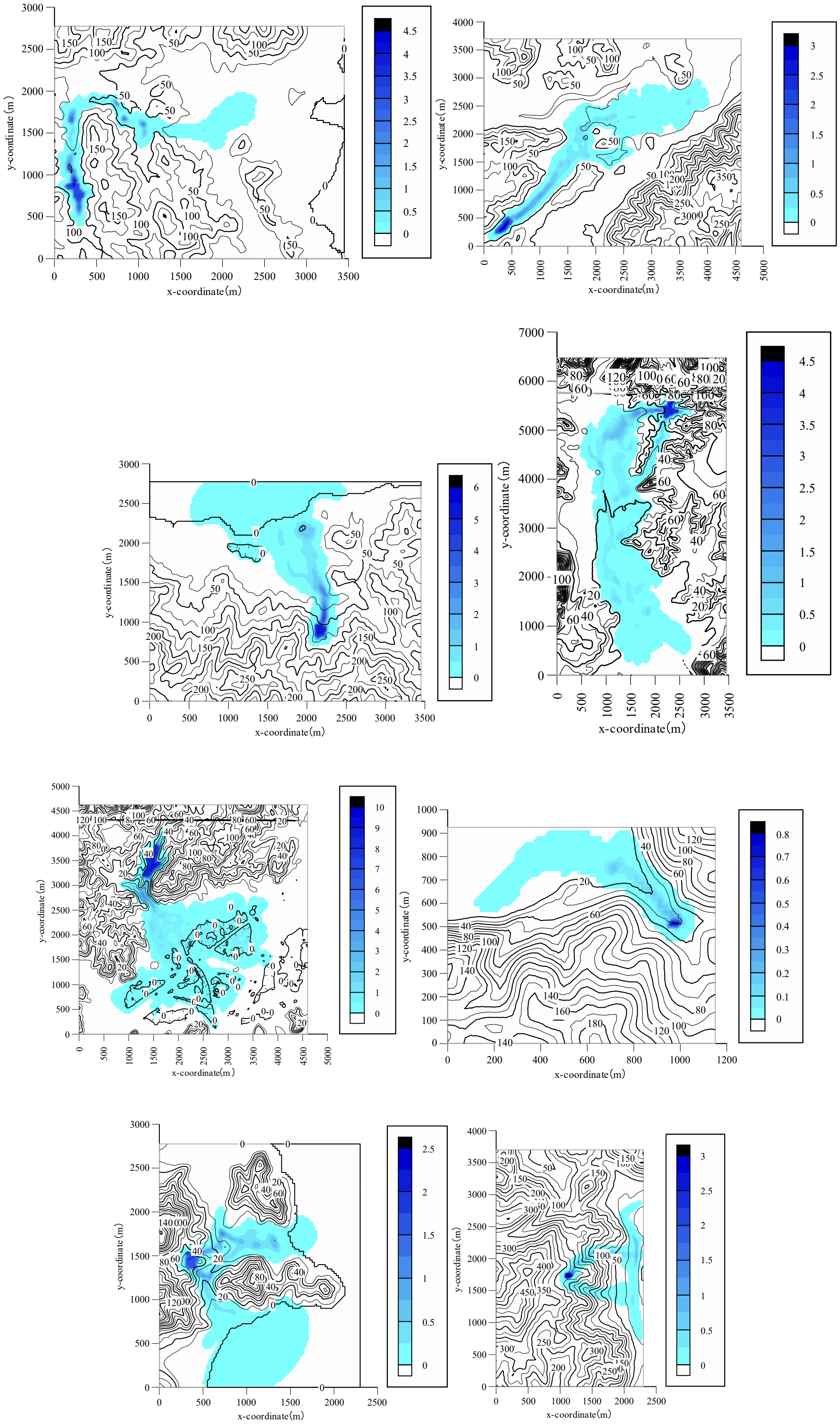

Figure A-1. Results of flooding area (Part5).

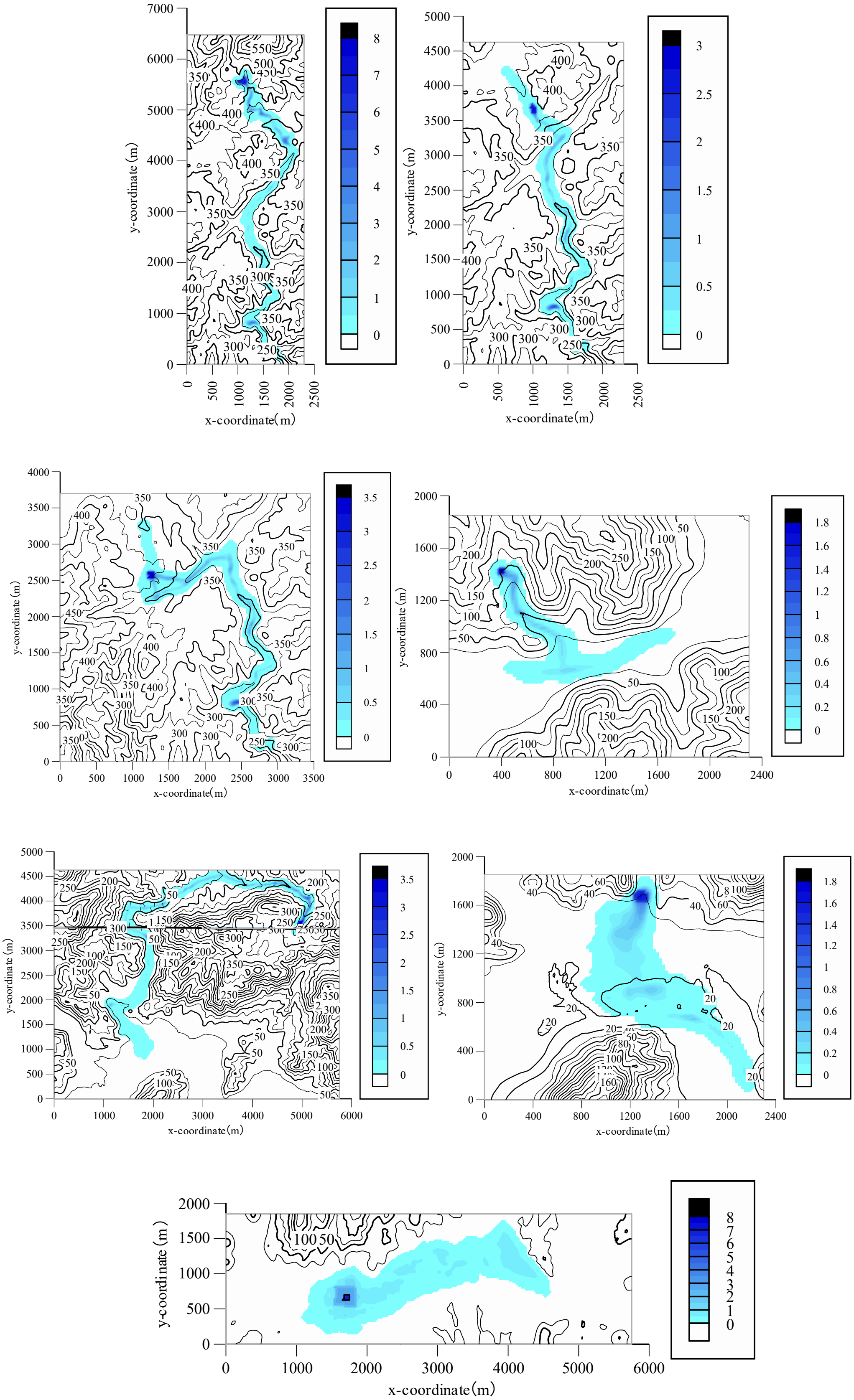

Figure A-1. Results of flooding area (Part6).

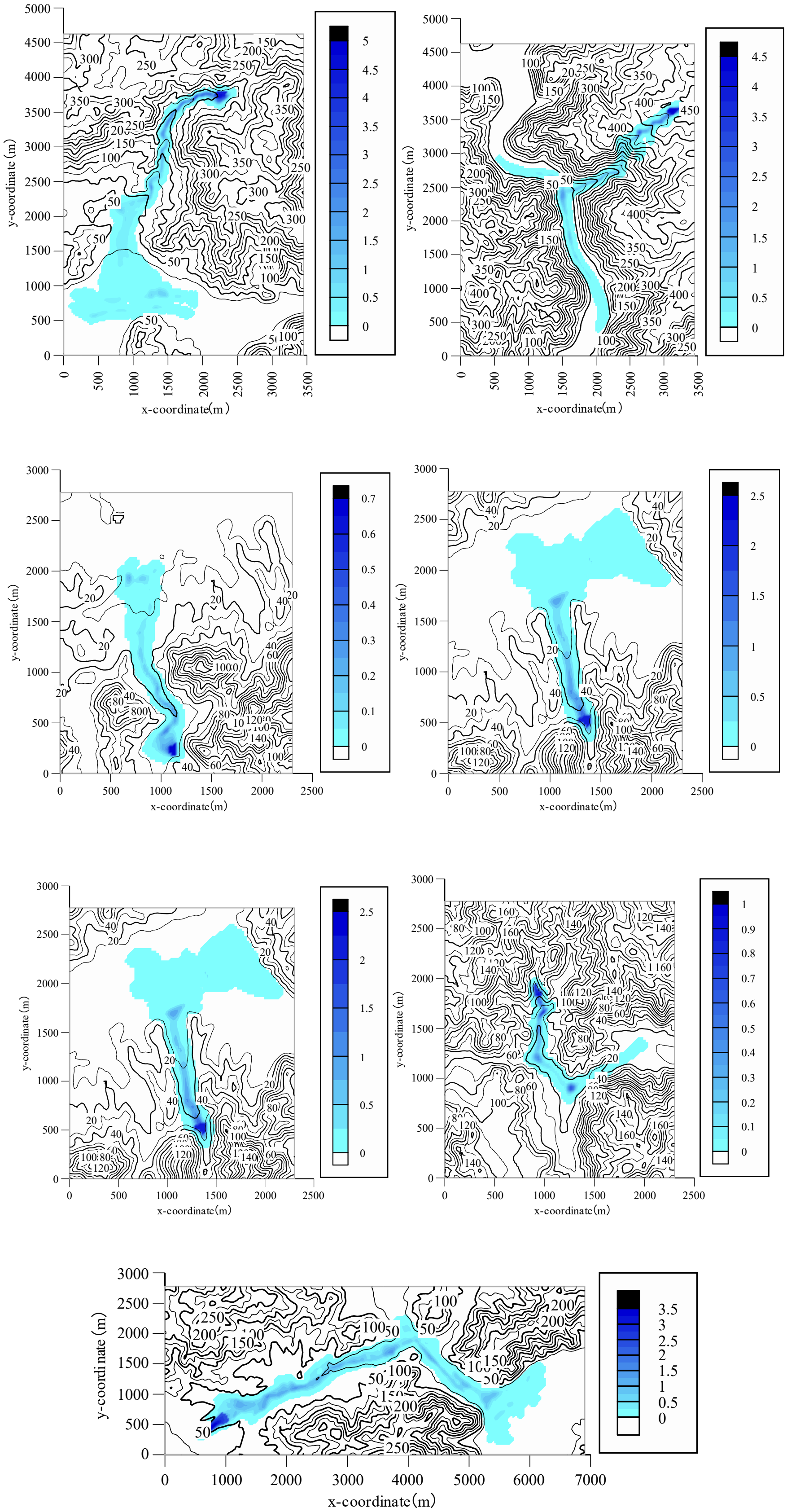

Figure A-1. Results of flooding area (Part7).

Result of risk analysis calculated by detailed method are shown in Table A-1.

Table A-1. Portion of earth-fill dams and results of risk assessment (Part1).

Site	Water storage	Design flow discharge	Damage cost	Overtopping probability	Risk
	(m^3)	(m^3/s)	(1,000 JPY)		(1,000JPY)
1	1000	1.0	58805	0.008	496.1
2	1019	11.3	1724120	0.003	4310.3
3	1095	0.1	3095600	0.003	7739.0
4	1890	2.2	5172340	0.003	12930.9
5	3000	2.5	316736	0.003	809.5
6	3100	3.0	4681480	0.003	11703.7
7	4000	1.3	5908620	0.015	89253.8
8	4500	0.6	252445	0.796	201029.8
9	5000	0.9	1922380	0.485	932740.7
10	5000	0.3	804178	1.000	804178.0
11	5300	0.4	2516580	0.348	876066.8
12	5625	1.1	8463840	0.993	8405007.8
13	6040	11.5	42482600	0.003	106206.5
14	7020	0.4	16002800	0.118	1882681.4
15	9500	1.8	13565300	0.008	105509.0
16	10000	0.4	3201220	0.206	660344.5
17	10300	2.6	4623110	0.003	11557.8
18	11000	6.6	539194	0.003	1348.0
19	12000	1.6	5970940	0.488	2912654.4
20	12000	0.4	3367720	0.080	268996.0
21	13000	7.0	391824	0.001	391.8
22	13700	0.2	169070	0.995	168228.9
23	14000	0.3	2538440	0.962	2440806.5
24	15000	0.7	2024690	0.003	5061.7
25	16000	2.8	8074670	0.001	8074.7

Table A-1. Portion of earth-fill dams and results of risk assessment (Part 2).

26	17000	0.8	6580370	0.003	16450.9
27	20000	0.6	458684	0.936	429391.1
28	22000	5.9	7311290	0.001	7311.3
29	24000	0.2	90100	0.001	90.1
30	24000	1.1	4304080	0.752	3234933.6
31	24000	26.1	317991	0.897	285339.7
32	24600	2.0	1747710	0.111	194189.8
33	25202	4.2	199725	0.003	499.3
34	26000	0.1	284355	0.467	132852.6
35	29000	2.2	6902080	0.217	1497199.2
36	29400	2.3	279750	0.020	5595.0
37	32000	0.1	1048450	0.003	2621.1
38	32000	4.7	599333	0.044	26299.2
39	33000	2.2	750668	0.025	19041.4
40	36000	0.9	1304000	0.415	541259.1
41	39000	2.1	35646	0.003	89.1
42	41000	2.2	3109040	0.285	887086.8
43	42000	0.8	26998500	0.158	4257285.5
44	43000	0.5	1752280	0.003	4380.7
45	43000	6.8	289090	0.003	722.7
46	49600	3.0	226511	0.003	566.3
47	50000	0.9	1625700	0.011	17441.8
48	51000	0.2	16680	0.426	7098.3
49	53000	9.6	2766950	0.001	2767.0
50	54000	4.4	6346560	0.001	6346.6

Table A-1. Portion of earth-fill dams and results of risk assessment (Part 3).

51	56000	2.1	1423280	0.087	124371.3
52	57000	1.3	2269950	0.003	5674.9
53	66210	2.0	5575840	0.045	253447.0
54	80000	0.0	6454700	0.984	6350798.7
55	92000	30.9	3110630	0.001	3110.6
56	107000	3.5	187117	0.002	352.9
57	109000	1.6	323990	0.081	26128.0
58	120000	6.2	32969400	0.001	32969.4
59	126000	6.9	2733370	0.034	91610.0
60	130000	49.6	3733550	0.003	9333.9
61	153000	3.8	5182840	0.004	21471.7
62	155400	2.9	13166500	0.003	32916.3
63	196000	68.9	13138300	0.003	32845.8
64	224000	2.0	16298300	0.116	1883333.8
65	226000	0.5	55109000	0.983	54149662.5
66	255000	25.4	12754800	0.004	54275.8
67	269000	3.4	28919600	0.018	519465.4
68	356000	17.3	25085200	0.007	172122.9
69	597000	9.5	45977300	0.005	251877.4
70	811000	3.6	54924300	0.377	20732495.2